# Spectropolarimetry for Satellite Identification

Louis Lischwe

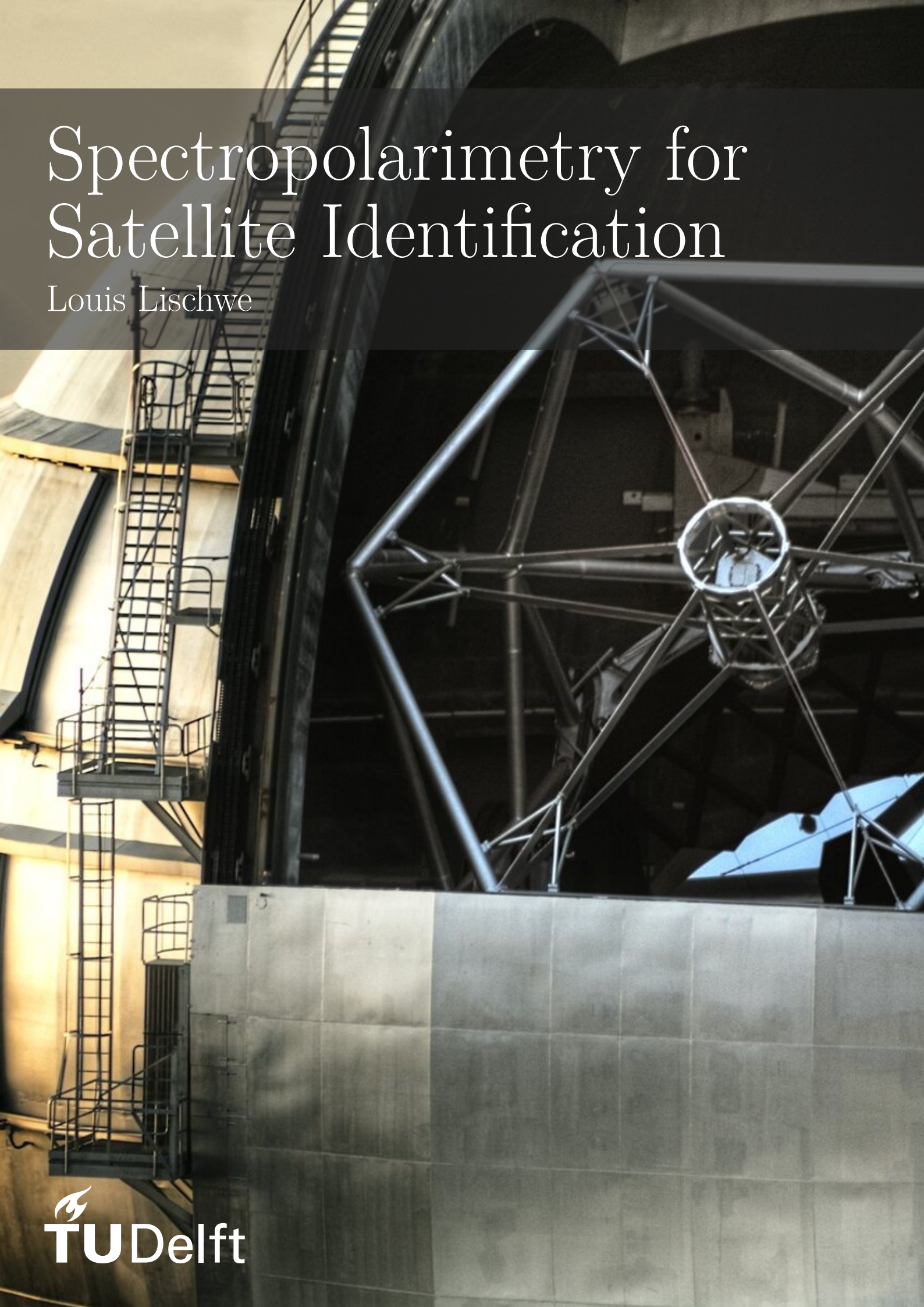

TU Delft

**23.09.2022**
**Delft, The Netherlands**

# Spectropolarimetry for Satellite Identification

by
Louis Lischwe
Faculty of Aerospace Engineering
Delft University of Technology

to obtain the degree of Master of Science in Aerospace Engineering,
at the Delft University of Technology

| | | |
|---|---|---|
| Student number: | 4443470 | |
| Thesis duration: | February 1, 2022 – October 7, 2022 | |
| Thesis committee: | Prof. dr. E.K.A. Gill, | TU Delft, chair |
| | Dr. ir. J.M. Kuiper, | TU Delft, responsible thesis supervisor |
| | Dr. D.M. Stam, | TU Delft, examiner |
| | Dr. T.P.G. Wijnen, | Leiden University, daily supervisor |

An electronic version of this thesis is available at
`http://repository.tudelft.nl/`.

cover image taken from https://www.esa.int/

TU Delft

# Preface

This thesis concludes my academic journey at the TU Delft over the last 7 years. It has not been easy but I do not regret taking that step. I really enjoyed working on the topic of spectropolarimetry. It was a totally new topic for me that I had not gotten into touch with during my studies. I learned a lot and would really enjoy to continuing this journey.
First of all, I would really like to thank my supervisors for the excellent support during the thesis. Especially the support in more challenging times motivated me to continue and work harder. Second, I would like to thank the staff of Leiden Observatory for the massive support and help with my work and the laboratory equipment. Last but not least, I want to thank TNO for the support and chance to take observations using their telescope.
I really hope I was able to contribute to the topic of space situational awareness and that the work on the spectropolarimeter for satellite identification will be successfully carried on.

Louis Lischwe

Not all those who wander are lost

# Abstract

The exponentially increasing number of Earth-orbiting satellites, as well as the pronounced importance for space military operations, impose new challenges on a functional Space Domain Awareness (SDA). A key factor for an effective SDA is the successful identification of an Earth-orbiting satellite, or object in general. Current methods are usually limited to either time-resolved photometry, spectrometry, or polarimetry. In this thesis, we present the Spectropolarimeter for Satellite Identification (SSI), whose design combines these detection methods with the aim to provide a unique 'fingerprint' of the satellite, thereby expanding the range of satellite identification methods.

The SSI combines a dual-channel spectrometer with off-the-shelf polarization optics. Using a combination of an achromatic quarter-wave retarder, a highly chromatic multiple order retarder, a polarizing beam splitter, and two linear polarizers, all operating in the visible spectrum, a sinusoidal modulation of the linear polarization information is imprinted onto the measured spectrum. The amplitude of the signal scales with the degree of linear polarization and the phase with the angle of linear polarization. Furthermore, by using a dual-channel setup, the intensity spectrum can be obtained for the full spectrograph resolution of 9 nm. We introduce and verify the retrieval algorithm to attain the linear polarization information with an approximate resolution of 135 nm due to the modulation approach. Differential transmission between both channels is corrected by a proposed iterative transmission correction which is verified to have an effect of $\leq 1\%$ on the accuracy of the retrieved linear polarization information.

This thesis concentrates on geostationary satellites as observation targets, making use of the stable observation geometry to simplify calibration and analysis. We reason that the phase angle has a strong influence on the retrieved spectropolarimetric data and received photon flux. A thorough photon budget estimation is conducted with the conclusion that we are able to observe faint geostationary satellites with an apparent visual magnitude of 10, especially if the observed phase angle is kept minimal.

An analysis of the most probable errors is conducted. We identify the convolution of the instrument response function with the modulated signal and the induced polarization by the telescope and instrument as the most severe ones. Laboratory wavelength and polarimetric calibration are conducted. Using a double glass plate setup to induce low levels of degree of linear polarization we performed laboratory validation measurements. We determined the overall laboratory polarimetric accuracy to be $\leq 1.2\%$. Additionally, we are able to distinguish signals $\geq 1.3$ %.

Preliminary observations of three bright stars are conducted. We are able to retrieve instrument-induced polarization between 1% and 2.5% which is in the expected range. We conclude that there has been a misalignment between the telescope and instrument which causes a large discrepancy between expected and received photons and propose future measures to resolve the issue.

The proof of concept to use linear channelled spectropolarimetry for satellite identification with the SSI will open up the way for further technical refinement of the instrument, an extension to low Earth orbit satellites, and the possible addition of phase angle resolved spectropolarimetric measurements to further improve the concept of a satellite's spectropolarimetric 'fingerprint'.



Our work is part of a collaboration between Leiden observatory and Delft University of Technology commissioned by the Royal Netherlands Air Force. Access to the telescope and support with the alignment activities were kindly provided by TNO.

# Table of Contents

# List of Figures

# List of Tables

# Nomenclature

| | |
|---|---|
| SSA | Space Situational Awareness |
| SDA | Space Domain Awareness |
| SSI | Spectropolarimeter for Satellite Identification |
| LEO | Low Earth Orbit |
| GEO | Geostationary Earth Orbit |
| DoLP | Degree of Linear Polarization |
| AoLP | Angle of Linear Polarization |
| CCD | Charge-Couple Device |
| TNO | Nederlandse Organisatie voor Toegepast Natuurwetenschappelijk Onderzoek |
| NORAD | North American Aerospace Defense |
| TLE | Two Line Element |
| SPEX | Spectropolarimeter for Planetary Exploration |

# 1 Introduction

The space domain in proximity to Earth has seen ever-increasing activity since the age of Sputnik 1 with exponential growth in the commercial and public sectors in recent years. Due to the more cost-effective access to space caused by the new private space economy, the number of artificial objects orbiting Earth is expected to increase from the order of $10^4$ today to $10^6$ in 2030 [12]. Simultaneously, space has become a military domain. Anti-satellite measures and compromising satellite manoeuvres of competitors force the NATO members to expand their military space capabilities [33]. This includes comprehensive Space Domain Awareness (SDA) and the capability of satellite identification [13]. Therefore, it is of high importance that industry and academia provide innovative and cost-effective sensors for future military SDA capabilities [9].

Satellite observation methods can be roughly divided into resolved and unresolved imaging. The performance of resolved imaging is limited by the diffraction limit of optical telescopes [52]. Resolved imaging of geostationary satellites (GEO) has been performed, but with poor resolution and the need for large aperture telescopes [24][15], making resolved imaging an unsuited method for a quick and cost-effective sensor expansion in the field of SDA. Multiple methods of unresolved imaging are available for satellite identification and characterisation. Photometry in varying complexity can be used to infer satellite characteristics [8][23]. Satellite identification has also been performed with a probability of success between 70-80 % [20][19]. Satellite spectrometry is mainly used to infer the composing materials and by that identify the satellite. Successful characterisation of space debris was conducted by Reddy et al. [37] using spectral observations. Especially the time-resolved spectral behaviour of satellites has been the target of extensive research [50][14][17]. In addition to photometry and spectrometry, polarimetry has mainly been used to infer geometry characteristics [5][6]. A successful identification of GEO satellites using polarimetry was conducted by Speicher [44].

The research of this thesis combines elements of unresolved satellite imaging by using spectropolarimetric measurements for satellite identification. Although, general spectropolarimetric measurements of satellites have been conducted recently [57], an attempt of using spectropolarimetric measurements for satellite identification in the field of SDA has not been performed before. This research is a combined effort of Leiden Observatory and Delft University of Technology commissioned by the Royal Netherlands Airforce to conduct a proof of concept for a spectropolarimeter for satellite identification.

**This thesis aims to answer the question if spectral linear polarization modulation in the form of channelled spectropolarimetry is able to recognize Earth-orbiting resident space objects.**

Chapter 2 depicts the chosen observation targets for this proof of concept. We concentrate on the observation of GEO satellites, trading brightness against a simple setup without the need for repetitive induced polarization calibration. Chapter 3 gives the theoretical background of the used method of spectral linear polarization modulation in the form of dual channelled spectropolarimetry based on the work of Snik et al. [42]. This snapshot method has the advantage of a straight forward instrument setup due to the absence of moving parts. The dual-channel setup can provide the intensity spectrum at full spectrograph resolution of 9 nm. Path differences are corrected by an iterative transmission algorithm. The degree and angle of linear polarization can be retrieved with an average reduced resolution of a factor of 15 due to the modulation approach. Chapter 4 presents the used instrument and its characteristics. To keep it simple and cost-effective, only off-the-shelf components are used for the instrument. Chapter 5 summarizes the laboratory calibration and testing activities. Finally, chapter 6 shows the results of preliminary observations and infers recommendations for future research.

We expect this research to be the base for a new category of satellite identification. That will provide our defence organisations with the strongly needed and cost-effective SDA sensors.

# 2 Targets and Observation Environment

The chapter at hand depicts the chosen observation targets as well as their location and movement. Additionally, an overview of the proposed alignment and calibration stars is given. The chapter ends with a description of the most important environmental factors influencing the observations.

## 2.1 Target Satellites

For the Spectropolarimeter for Satellite Identification's (SSI) proof of concept, it was decided to concentrate on the observation of GEO satellites. The trade-off between GEO satellites and other lower Earth-orbiting targets was mainly influenced by the stability of the observation geometry for GEO satellites. The retrieved polarization information of an Earth-orbiting object is strongly dependent on the illumination geometry [57][11][4]. Therefore, a relatively stable illumination geometry as for GEO satellites aids in not mixing up polarization effects for longer integration times. Additionally, the calibration for instrument-induced polarization is simplified. On the other hand, GEO satellites have reduced apparent brightness due to their high orbit altitude. Therefore, longer integration times will be needed as compared to lower Earth-orbiting objects. Table 1 depicts the chosen targets with their name and NORAD catalogue number.

Table 1: Satellite Targets with their name and NORAD catalogue number.

| **Target Satellites** | | | |
|---|---|---|---|
| NIGCOMSAT 1 (31395) | ASTRA 1N (37775) | ASTRA 3B (36581) | ASTRA 1L (31306) |
| ASTRA 1KR (29055) | ARABSAT 4B (29526) | SKYNET 5B (32294) | YAHSAT 1B (38245) |
| SBIRS GEO 2 (USA 241) (39120) | USA 164 (27168) | EUTE 36B (EUTE W7) (36101) | BADR-5 (ARABSAT 5B) (36592) |
| BADR 7 (41029) | BADR 6 (33154) | ASTRA 1M (33436) | EUTE 28B (EUTE W2M) (33460) |
| THURAYA 2 (27825) | | | |

The targets were chosen based on their visibility from the Netherlands and relatively good apparent visual brightness for a GEO satellite ranging around $10\mp2$. We expect the degree of linear polarization to range between 0-0.2. The needed accuracy could not be deducted from the literature [57][44]. The position and movement of each GEO satellite is determined from the Two Line Element (TLE). For each night of observation, the most actual TLE´s are downloaded and fed to a Python script based on the Skyfield module calculating and propagating their position and illumination conditions [43]. The recency of the estimations is checked by the TLE listed epoch of observation. Subsequently, the TLEs are fed to the telescope software enabling initial pointing and tracking.
As an example, for 20.09.2022 the location of each GEO satellite given in longitude and latitude is shown in Fig. 1b. The target coordinates in azimuth and elevation are shown in Fig. 1a. It can be seen, that most satellites are located in the southeast and two in the southwest. The elevation ranges from 18° to 36° degrees. The elevation angle has a strong influence on the scattering and extinction by the atmosphere and therefore on the received flux. The influence is modelled in section 2.3.

A GEO orbit is theoretically circular and located at an orbit altitude of 35786 km with an orbital period of 1436 minutes and an inclination of 0° degrees directly above the Earth's equator. However, the actual orbit will deviate from the theoretical parameters. This will result in a daily perceived elliptical or analemma movement in the sky. For a difference in inclination, the height of this apparent movement is given by equation 1a and the width by equation 1b. The width of the movement ellipse for a minor eccentricity is given by equation 1c [51].

Taking the Skynet 5 B GEO satellite with an inclination of $\pm 1.03°$ degrees and nearly 0 eccentricity as an example results in a width of the movement ellipse of $\pm 4.6 \cdot 10^{-3}$ degrees and a height of $\pm 1.03°$ degrees over one orbital period. With the telescope being able to track a target with a slew speed of up to 50° degrees per second, this does not pose any problem for the observations [2].

$$\text{height}_{inc} = \pm i \tag{1a}$$

$$\text{width}_{inc} = \pm \left(\frac{i}{4}\right) \sin i \tag{1b}$$

$$\text{width}_{ecc} = \pm 2e \tag{1c}$$

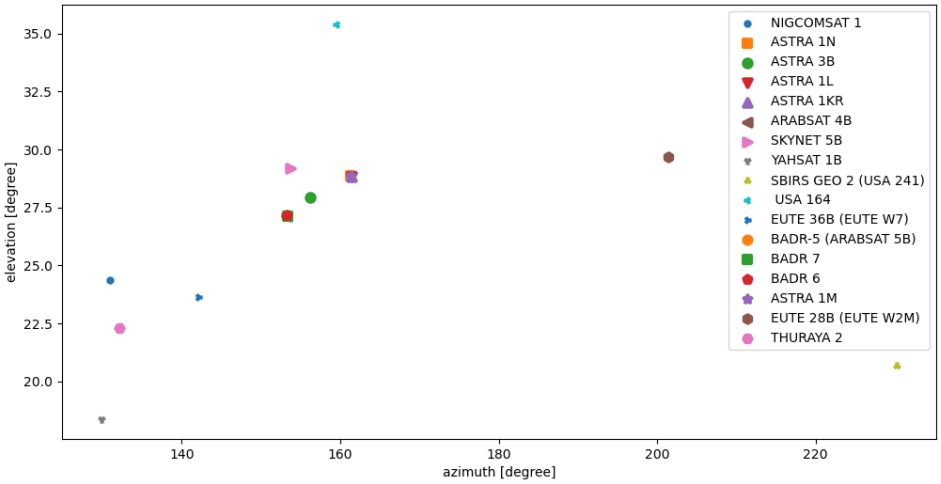


(a)

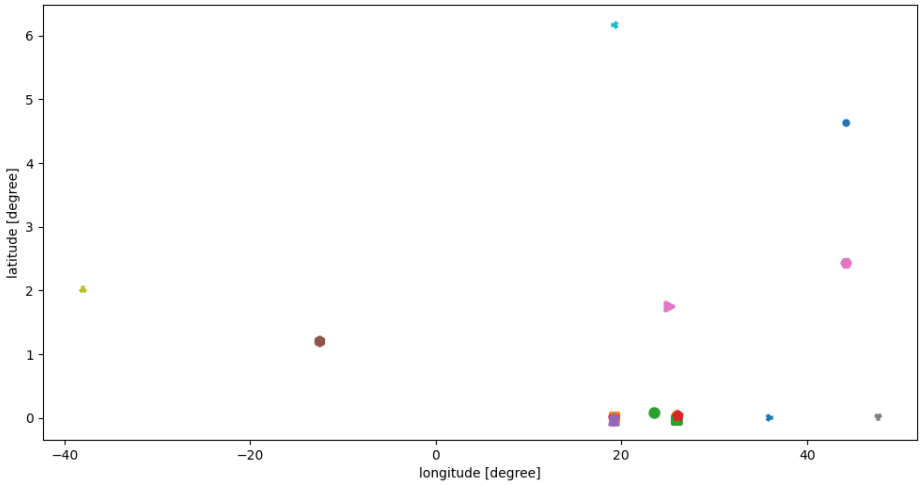


(b)

Figure 1: Satellite target position in azimuth-elevation and longitude-latitude coordinates (20.09.2022).

## 2.2 Alignment and Calibration Targets

In order to calibrate the SSI for instrument-induced polarization, calibration targets with known linear polarization are needed. Additionally, those targets can serve as alignment targets. As instrument-induced errors will vary with the pointing direction of the telescope, the calibration targets have to be spread out over the whole possible viewing field. As an example, for 20.09.2022 the position of the calibration stars in azimuth and elevation are depicted in Fig. 2.

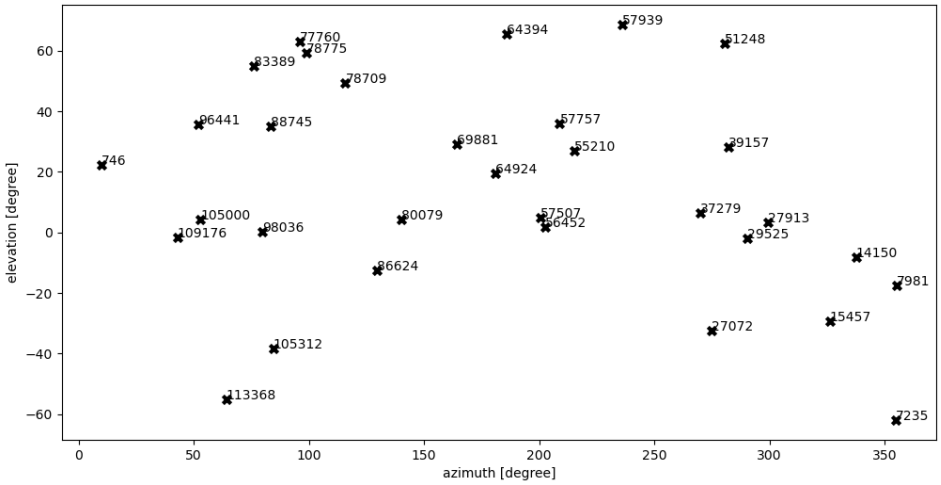


Figure 2: Calibration target location in azimuth-elevation coordinates. Hipparcos star catalogue numbering used.

The calibration targets are distributed over a large elevation and azimuth range, their visual apparent magnitude is known, as well as their linear polarization [28]. As the stars will move over the sky due to the Earth's rotation and its movement around the Sun, their position has to be updated right before each observation to determine the best-suited calibration target. This is done by downloading their International Celestial Reference System coordinates and propagating them to the desired point in time.

## 2.3 Observation Environment and Geometry

In the first step, one has to determine if the target is visible or in the Earth's shadow. This is done prior to every observation night propagating the viewing geometry for each satellite using a Python script based on the Skyfield module. An example shown in Fig. 3a.

The illumination geometry, more precise the phase angle, has an enormous effect on the spectral reflectance and the polarization response of the satellite. A simplified 2-d representation of the phase angle can be seen in Fig. 4. It is simply the angle between the two lines, one connecting the sun and the target, and the second connecting the target and the location of observation. In reality, the phase angle will differ for the various components of the satellite, as it is not a plane surface area with constant orientation. Also, the phase angle will depend on the season of observation, the precise orbit of the target, and the latitude and longitude of the observation location [44]. The intensity spectrum of the satellite will change throughout the progression of the phase angle with time, with an accelerated change close to a phase angle of 0° degrees corresponding to the highest flux one can observe. At a phase angle of close to 0° degrees, a glint will occur. A glint is a spike in reflected light. Usually, a glint of a satellite is attributed to an intensity spike due to the solar panels. As for a three-axis stabilized satellite the solar panels will be arranged normal to the sun to maximize the power output, and the corresponding phase angle for a glint will be 0° degrees [50].

For a GEO satellite, this intensity spike also depends on the season and will be maximum twice a year at equinox as estimated by simulations of Murray-Krezan et al. [32]. Therefore, it is advantageous to observe the GEO satellites at low phase angles to gain as many photons as possible. The phase angle progression for all GEO target satellites for the night of 20.09.2022 is shown in Fig. 3b. Most of the satellites are best observed at the beginning of the night, whereas the two southwest located satellites are best observed around midnight.

Next to the illumination geometry, the radiation propagation through the Earth's atmosphere is another important factor influencing the measurements. Radiation travelling through the atmosphere can be extinct by absorption and scattering. Atmospheric extinction can affect the overall flux, the spectrum, and the polarization state of the electromagnetic light wave depending on the mode of extinction. Atmospheric absorption has a large effect on the spectrum. Earth's atmosphere features several absorption patterns due to molecules like $O_3$ and $H_2O$, also in the visible wavelength regime, which will alter the retrieved spectrum [30]. Scattering due to smaller molecules, Rayleigh scattering, and due to larger particles, Mie scattering, both affect the spectrum as they are wavelength-dependent [39]. Mie scattering is mostly forward scattering and it can be assumed that the linear polarization information is conserved. The effect of Rayleigh scattering on the linear polarization information has a positive correlation with the scattering angle. As the targets are directly observed we assume that the scattering angle is negligible and mainly forward scattered light is observed. Therefore, for the proof of concept, it is assumed that linear polarization is only minimally affected, such that calibration measures can be neglected [44][40]. It is recommended to further analyse the atmospheric effects using standard calibration stars for enhanced accuracy of the spectropolarimetric measurements.
The overall extinction of the atmosphere due to absorption and scattering increases the apparent visual magnitude and thereby reduces the received flux of a target. The reduction in brightness depends on the wavelength-dependent atmospheric extinction coefficient $\kappa(\lambda)$ and the air mass X(z) as shown by equation 2. The air mass can be calculated as a function of the zenith angle as given by equation 3. The zenith angle is defined as the angle between the location of the target and the zenith. The horizon does therefore have a zenith angle of 90° degrees. The atmospheric extinction coefficient largely depends on the aerosol content of the air and the relative humidity [56].

$$m(\lambda) = m_0(\lambda) + \kappa(\lambda)X(z) \tag{2}$$

$$X = \sec z \left(1 - 0.0012 \left(\sec^2 z - 1\right)\right) \tag{3}$$

It becomes obvious that the atmospheric influence on light propagation is highly influenced by the location of observation. The telescope is situated in The Hague in the proximity of the ocean, which could increase the relative humidity of the air and thereby the extinction coefficient. Additionally, figure 1a depicts the target satellites mainly located in the south with a relative low elevation over the horizon. Apart from a higher expected air mass, this also increases background radiation and stray light due to the light pollution of the city of The Hague.

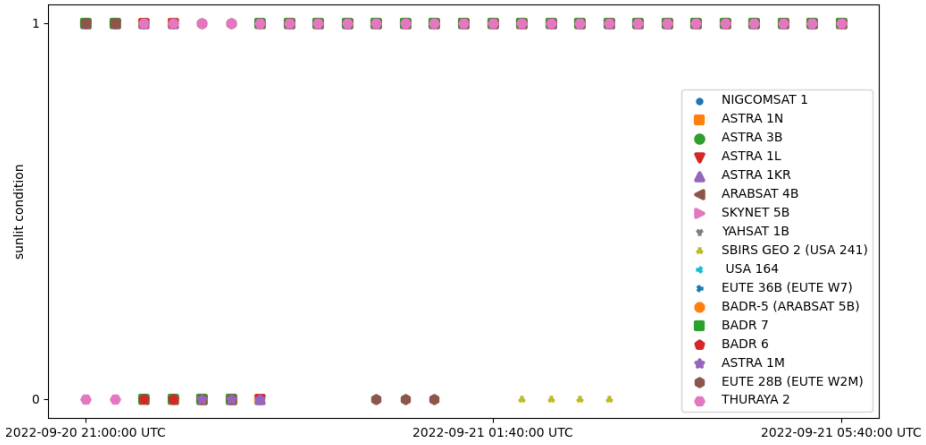


(a)

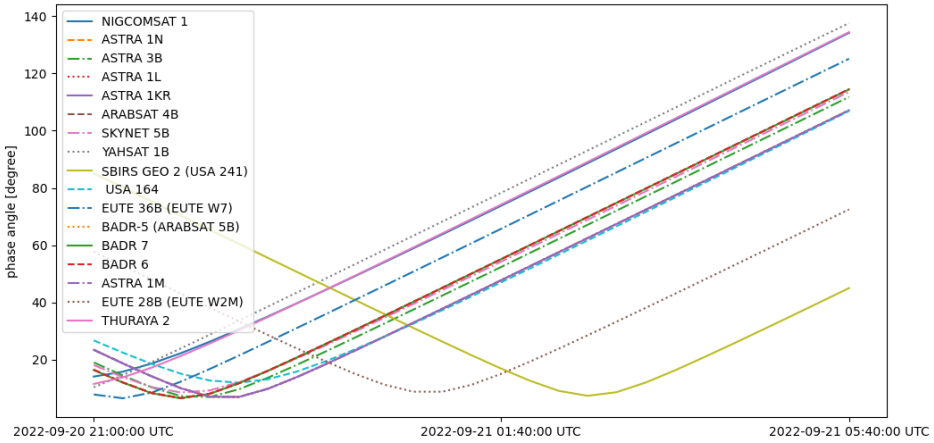


(b)

Figure 3: Target satellite visibility and phase angle progression for the night of 20.09.2022.

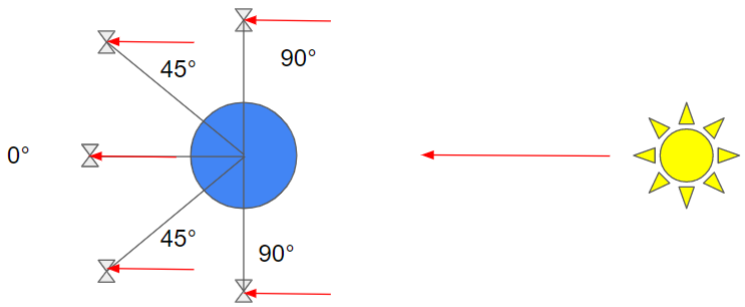


Figure 4: 2-d Phase angle geometry based on Speicher [44].

# 3 Theoretical Background and Data Processing

This chapter derives and describes the used modulation principle. Subsequently, the polarization information retrieval algorithm is explained.

## 3.1 Modulation Principle

The SSI facilitates a method of channelled spectropolarimetry modulation capturing the linear polarization information as also used by the Spectropolarimeter for Planetary Exploration (SPEX) instrument prototype [26][42].
It is common to describe the polarization of an electromagnetic wave using the Stokes vector formalism [45]. Manipulation of Stokes vector components is best expressed using Mueller matrix calculus. The Stokes vector $\vec{S} = [I, Q, U, V]$ summarizes the orientation of the electromagnetic wave in space using four components. The meaning of each component becomes clear by explaining how each component is measured using a sequence of a linear retarder and a linear polarizer. A linear retarder imparts a phase lag $\delta$ on the incoming electromagnetic vector denoted by its Cartesian components $E_x$ and $E_x$ in Fig. 5. The linear retarder has a slow and fast axis being perpendicular to each other. The retardance is only applied through the slow axis, while incoming vector components being parallel to the fast axis do not experience a phase lag. The linear polarizer transmits all light passing through its optical axis and extinguishes all other vector components. The angle between the optical axis and the Cartesian coordinate system in which the electromagnetic vector is defined is depicted in Fig. 5 by $\theta$. The Stokes vector components can now be measured by using the sequence of linear retarder and linear polarizer with varying $(\theta, \delta)$ as given by equation 4 [47].

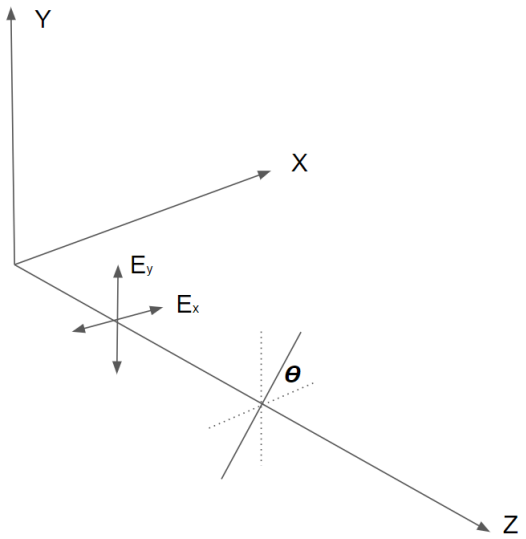


Figure 5: Schematic of electromagnetic wave vector components and an optical axis [47].

Following this measurement formalism, [I] represents the total received flux, [Q] the tendency of the electromagnetic vector orientation with respect to the Cartesian coordinate system of 0° over 90° degrees, [U] of 45° over 135° degrees, and [V] represents the difference between the right- and left-handed circular polarization. The degree of linear polarization (DolP) and angle of linear polarization (AolP) are then defined by equations 5a and 5b.

$$
\begin{aligned}
I &= I_{\text{meas}}\,(0,0) + I_{\text{meas}}\,(\pi/2,0) \\
Q &= I_{\text{meas}}\,(0,0) - I_{\text{meas}}\,(\pi/2,0) \\
U &= I_{\text{meas}}\,(\pi/4,0) - I_{\text{meas}}\,(3\pi/4,0) \\
V &= I_{\text{meas}}\,(\pi/4,\pi/2) - I_{\text{meas}}\,(3\pi/4,\pi/2)
\end{aligned}
\tag{4}
$$

$$
P_L = \frac{\sqrt{Q^2+U^2}}{I} \tag{5a}
$$

$$
\phi = \frac{1}{2} tan^{-1}\left(\frac{U}{Q}\right) \tag{5b}
$$

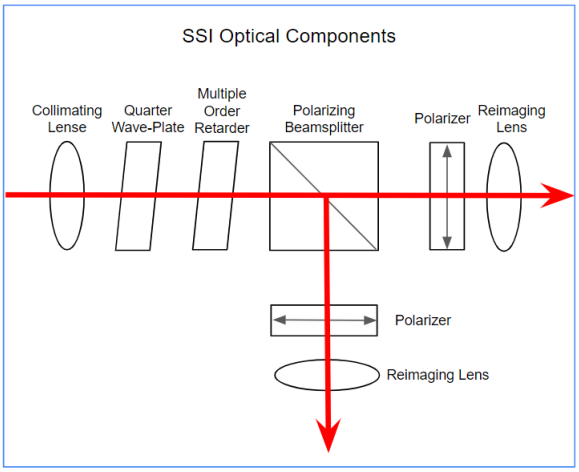


Figure 6: Schematic of the used optical components for the instrument.

A schematic of the SSI optical components used for the modulation method is given in Fig. 6. The modulation method makes use of an optical train consisting of an achromatic quarter-wave retarder, a multiple-order retarder, and a polarizing beamsplitter. For each light beam, the polarizing beamsplitter is followed by a linear polarizer with its optical axis aligned with the respective light beam's polarization state to filter out remaining orthogonally polarized light after the beamsplitter [42]. The polarizing beamsplitter splits the incoming light into a p- and s-polarized beam being orthogonal to each other. This denotation is used to describe the orientation of polarization, or that of the optical axis of the respective linear polarizer, with the principle reference axis of the light propagating through the instrument, represented by the z-axis in Fig. 5. Using again Fig. 5 as a reference, the p-polarized beam would be parallel with the x-axis, and the s-polarized beam with the y-axis.

The linear transformation of the Stokes vector in $\mathbb{R}^4$ is described by the $4 \times 4$ Mueller matrix as depicted by equation 6.

$$
\begin{pmatrix} I' \\ Q' \\ U' \\ V' \end{pmatrix} = \begin{pmatrix} M_{00} & M_{01} & M_{02} & M_{03} \\ M_{10} & M_{11} & M_{12} & M_{13} \\ M_{20} & M_{21} & M_{22} & M_{23} \\ M_{30} & M_{31} & M_{32} & M_{33} \end{pmatrix} \begin{pmatrix} I \\ Q \\ U \\ V \end{pmatrix} \tag{6}
$$

Every piece of optics is represented by its own Mueller matrix. The resulting Mueller matrix of the whole system of $n$ components is represented by equation 7 adhering to the rules of matrix multiplication. $M_1$ is the first optical component encountered by the light beam and $M_n$ is the last as seen along the direction of propagation.

$$M_{system} = M_n M_{n-1} ... M_2 M_1 \tag{7}$$

The first polarization optics used in the optical train is an achromatic quarter-wave retarder. Denoting $c_2 = \cos 2\theta$ and $s_2 = \sin 2\theta$, with $\theta$ being the angle between the positive x-axis and the fast axis of the retarder, the general Mueller matrix for a linear retarder of retardance $\delta$ is given by equation 8.

$$\vec{R}(\theta, \delta) = \begin{pmatrix} 1 & 0 & 0 & 0 \\ 0 & c_2^2 + S_2^2 cos\delta & c_2 s_2 (1 - cos\delta) & -s_2 sin\delta \\ 0 & c_2 s_2 (1 - cos\delta) & s_2^2 + c_2^2 cos\delta & c_2 sin\delta \\ 0 & s_2 sin\delta & -c_2 sin\delta & cos\delta \end{pmatrix} \tag{8}$$

The used achromatic quarter-wave retarder features a retardance of $\pi/2$ and its fast axis is aligned with the positive x-axis or +Q axis. Therefore, the resulting Mueller matrix is represented by equation 9 [47][36].

$$\vec{R}(0, \pi/2) = \begin{pmatrix} 1 & 0 & 0 & 0 \\ 0 & 1 & 0 & 0 \\ 0 & 0 & 0 & 1 \\ 0 & 0 & -1 & 0 \end{pmatrix} \tag{9}$$

The second optical component is the multiple-order retarder. The multiple order retarder is oriented at $-45°$ degrees with an overall retardance of $\delta(\lambda)$. The retardance is wavelength-dependent, as the multiple-order retarder is chosen to be highly chromatic. Applying the characteristics to equation 8 leads to the Mueller matrix for the chromatic multiple-order retarder as shown by equation 10 [47][36][42].

$$\vec{R}(-\pi/4, \delta(\lambda)) = \begin{pmatrix} 1 & 0 & 0 & 0 \\ 0 & cos\delta(\lambda) & 0 & sin\delta(\lambda) \\ 0 & 0 & 1 & 0 \\ 0 & -sin\delta(\lambda) & 0 & cos\delta(\lambda) \end{pmatrix} \tag{10}$$

The last optical component is the polarizing beamsplitter. The polarizing beamsplitter acts as a linear polarizer for both polarization states, the p- and s-polarized beam. The general form of the Mueller matrix for a linear polarizer with its optical axis at an angle $\theta$ with respect to the x-axis is given by equation 11 [47][36].

$$L(\theta) = \frac{1}{2} \begin{pmatrix} 1 & cos2\theta & sin2\theta & 0 \\ cos2\theta & cos^2 2\theta & cos2\theta sin2\theta & 0 \\ sin2\theta & cos2\theta sin2\theta & sin^2 2\theta & 0 \\ 0 & 0 & 0 & 0 \end{pmatrix} \tag{11}$$

$$L(0 \| \pi/2) = \frac{1}{2} \begin{pmatrix} 1 & \pm 1 & 0 & 0 \\ \pm 1 & 1 & 0 & 0 \\ 0 & 0 & 0 & 0 \\ 0 & 0 & 0 & 0 \end{pmatrix} \tag{12}$$

The actual Mueller matrix for the linear polarizers is depicted by equation 12. Combining the matrices according to equation 7 results in the Mueller matrix of the optical train shown by equation 13. The value of k is 1 for the p-polarized channel and $-1$ for the s-polarized channel.

$$\frac{1}{2}\begin{pmatrix} 1 & k\cos\left(\frac{2\pi\delta}{\lambda}\right) & -k\sin\left(\frac{2\pi\delta}{\lambda}\right) & 0 \\ k & \cos\left(\frac{2\pi\delta}{\lambda}\right) & -\sin\left(\frac{2\pi\delta}{\lambda}\right) & 0 \\ 0 & 0 & 0 & 0 \\ 0 & 0 & 0 & 0 \end{pmatrix}, \quad k = +1, -1, \tag{13}$$

Combining the instrument Mueller matrix with the Stokes vector of the incoming unmodulated beam results in the modulated Stokes vector shown by equation 14.

$$\begin{pmatrix} I(\lambda) \\ Q(\lambda) \\ U(\lambda) \\ V(\lambda) \end{pmatrix} = \frac{1}{2}\begin{pmatrix} I_0(\lambda) + Q_0(\lambda)\, k\cos\left(\frac{2\pi\delta}{\lambda}\right) - U_0(\lambda)\, k\sin\left(\frac{2\pi\delta}{\lambda}\right) \\ I_0(\lambda)\, k + Q_0(\lambda)\, \cos\left(\frac{2\pi\delta}{\lambda}\right) - U_0(\lambda)\, \sin\left(\frac{2\pi\delta}{\lambda}\right) \\ 0 \\ 0 \end{pmatrix} \tag{14}$$

The measured modulated signals of the p- and s-polarized channel by the spectrometer are then given by equations 15 and 16 respectively, where q and u are the normalized Stokes vector components [41].

$$I_p(\lambda) = \frac{1}{2} I_0(\lambda) \left\{ 1 + q(\lambda) \cos\left(\frac{2\pi\delta}{\lambda}\right) - u(\lambda) \sin\left(\frac{2\pi\delta}{\lambda}\right) \right\} \tag{15}$$

$$I_s(\lambda) = \frac{1}{2} I_0(\lambda) \left\{ 1 - q(\lambda) \cos\left(\frac{2\pi\delta}{\lambda}\right) + u(\lambda) \sin\left(\frac{2\pi\delta}{\lambda}\right) \right\} \tag{16}$$

The modulation equations can be further simplified by mathematical manipulations shown by the following equations for the p-polarized channel.

$$I(\lambda) = \frac{1}{2} I_0 (1 + \frac{\sqrt{Q_0^2 + U_0^2}}{I_0} (\frac{cos\delta(\lambda)}{\sqrt{\frac{U_0^2}{Q_0^2} + 1}} - \frac{U_0 sin\delta(\lambda)}{Q_0 \sqrt{\frac{U_0^2}{Q_0^2} + 1}})) \tag{17a}$$

$$sin(tan^{-1}(\frac{U_0}{Q_0})) = \frac{\frac{U_0}{Q_0}}{\sqrt{\frac{U_0^2}{Q_0^2} + 1}} \tag{17b}$$

$$cos(tan^{-1}(\frac{U_0}{Q_0})) = \frac{1}{\sqrt{\frac{U_0^2}{Q_0^2} + 1}} \tag{17c}$$

$$I(\lambda) = \frac{1}{2} I_0 (1 + \frac{\sqrt{Q_0^2 + U_0^2}}{I_0} (cos\delta(\lambda) cos(tan^{-1}(\frac{U_0}{Q_0})) - sin\delta(\lambda) sin(tan^{-1}(\frac{U_0}{Q_0})))) \tag{17d}$$

$$cos(\delta(\lambda) + tan^{-1}(\frac{U_0}{Q_0})) = cos\delta(\lambda) cos(tan^{-1}(\frac{U_0}{Q_0})) - sin\delta(\lambda) sin(tan^{-1}(\frac{U_0}{Q_0}) \tag{17e}$$

$$I(\lambda) = \frac{1}{2} I_0 (1 + \frac{\sqrt{Q_0^2 + U_0^2}}{I_0} cos(\delta(\lambda) + tan^{-1}(\frac{U_0}{Q_0}))) \tag{17f}$$

$$I_{p/s}(\lambda) = \frac{1}{2} I_0(\lambda) t(\lambda)_{p/s} \left\{ 1 \pm \mathrm{P_L}(\lambda) \cos\left(\frac{2\pi\delta(\lambda)}{\lambda} + 2\,\phi(\lambda)\right) \right\} \tag{18}$$

Equation 16 is multiplied by $\frac{\sqrt{Q_0^2+U_0^2}}{\sqrt{Q_0^2+U_0^2}}$ to achieve equation 17a. Using the trigonometric identities given by equations 17b and 17c leads to the representation for the intensity as given by equation 17d. Applying the angle sum identity given by equation 17e results in equation 17f. Finally, using the definitions for the DoLP and AoLP depicted in equation 5a and 5b gives the final result for the wavelength-dependent intensity modulation shown by equation 18 [42][36]. The differential transmission between the p- and s-polarized channel is given by $t(\lambda)_{p/s}$.

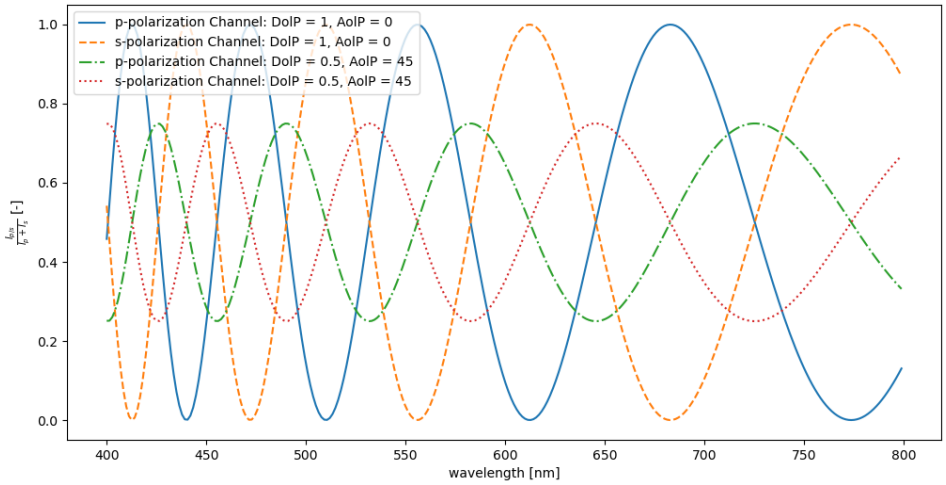


(a)

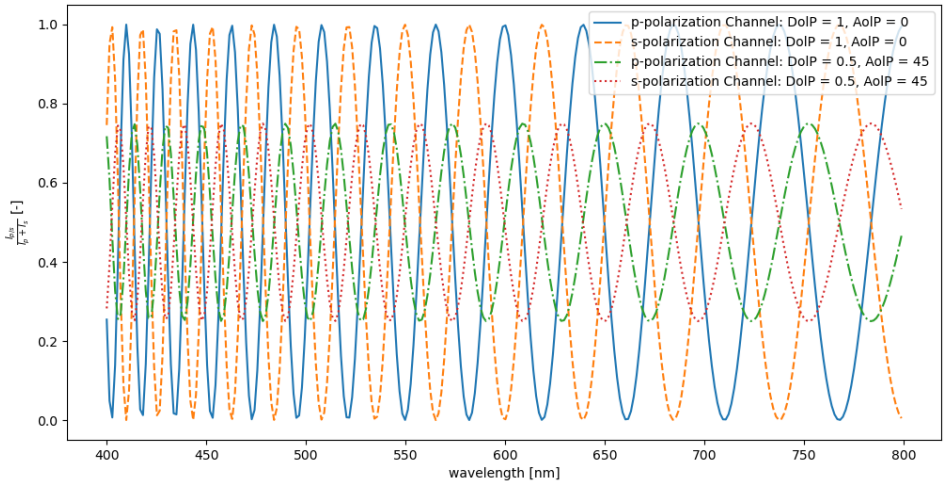


(b)

Figure 7: Relative modulation signal for DoLP = 1/AoLP = 0° degrees and DoLP = 0.5/AoLP = 45° degrees. Modulation in (a) has an average local modulation period of 135 nm. Modulation in (b) has an average local modulation period of 40 nm.

An example of the modulation principle is given in Fig. 7a. The relative modulation signal for both channels after the division of equation 18 by $I_0$ is shown. The high amplitude modulation is simulated with a DoLP = 1 and AoLP = 0° degrees. The lower amplitude modulation is simulated with a DoLP = 0.5 and AoLP = 45° degrees. The modelling was conducted with the characteristics of the multiple-order retarder used in the actual SSI setup. For the shown wavelength range of 400 - 800 nm, this corresponds to an average local modulation period of 135 nm. The decrease in amplitude and shift in phase are clearly visible.
A similar simulation, only increasing the retardance of the multiple-order retarder by a factor of 3 is depicted in Fig 7b. The average local modulation period is now decreased to 40 nm. This clearly shows the influence of the retardance of the multiple-order retarder on the resolution of the retrievable polarization information.

## 3.2 Retrieval Algorithm

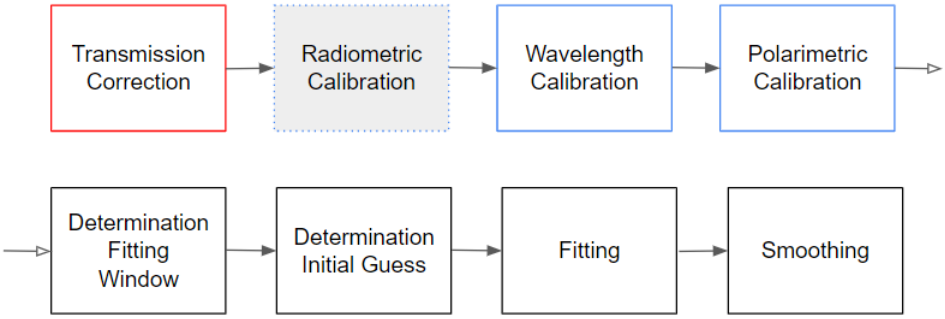


Figure 8: Schematic of retrieval algorithm for the linear polarization information.

Fig. 8 gives an overview of the retrieval algorithm to extract the linear polarization information modulated onto the measured spectrum. The algorithm can be divided into operations for iterative transmission correction (red), calibration measures (blue), and fitting operations (black). This section concentrates on transmission correction and fitting operations. The calibration measures and results are shown in section 5.

### Transmission Correction

An exact determination of the differential transmission of both channels is hard to determine due to the off-the-shelf nature of the instrument. The reimaging lenses depicted in Fig. 6 are highly sensitive to misalignment of the incoming beam. As the instrument is constructed such that the optical components are easily removable, slight vibrations can cause misalignment. In addition, transmission per channel is prone to change with time and can change for every observation with the telescope. Therefore, an iterative transmission correction is applied.
The normalized difference between both channels is given by equation 19, where $t(\lambda)$ is defined as $\frac{t(\lambda)_s}{t(\lambda)_p}$. The equation is used to perform a fit to the measured normalized difference over one modulation period. The difference to the measured normalized difference can be attributed to the higher frequency components of the transmission difference and can be corrected. Iteratively varying the upper bound for $\mathrm{P_L}(\lambda)$ based on the variance of $\phi$ prevents a false modulation of $\mathrm{P_L}(\lambda)$ for a non-smooth transmission difference and allows the algorithm to converge to the true $t(\lambda)$.

$$\frac{\frac{1}{2}\left\{1+\mathrm{P_L}(\lambda)\cos\left(\frac{2\pi\delta(\lambda)}{\lambda}+2\,\phi(\lambda)\right)\right\}-\frac{1}{2}t(\lambda)\left\{1-\mathrm{P_L}(\lambda)\cos\left(\frac{2\pi\delta(\lambda)}{\lambda}+2\,\phi(\lambda)\right)\right\}}{\frac{1}{2}\left\{1+\mathrm{P_L}(\lambda)\cos\left(\frac{2\pi\delta(\lambda)}{\lambda}+2\,\phi(\lambda)\right)\right\}+\frac{1}{2}t(\lambda)\left\{1-\mathrm{P_L}(\lambda)\cos\left(\frac{2\pi\delta(\lambda)}{\lambda}+2\,\phi(\lambda)\right)\right\}} \tag{19}$$

### Fitting Operations

The general idea of the retrieval algorithm is to create a spectral window for which the polarization information is estimated by fitting equation 15 or 16 to the measured intensity data points.
For each wavelength point measured by the spectrograph, a spectral window is created with the data point as the centre. The spectral window should be at least the width of the local modulation periodicity for a good fit of the cosine function to be estimated. As the modulation is not periodic in $\lambda$, but in $\frac{1}{\lambda}$, and the retardance $\delta(\lambda, T)$ is itself a function of wavelength, there is not going to be a fixed period when analysing the modulated spectrum. The local modulation period is given by equation 20 and can be reduced to $\frac{\lambda^2}{\delta}$ for $\delta >> \lambda$. Therefore, the width of the spectral window is quadratic in wavelength and will grow with the local modulation period as the wavelength shifts to the red.

Some spectral windows located at the edges of the measured spectrum will therefore not have full coverage of data points and are omitted. Therefore, polarization information at the edges of the spectrum will be lost.

$$\Delta\lambda = \frac{\lambda^2}{\delta(1 + \frac{\lambda^2}{4\delta^2})} \tag{20}$$

Table 2: Coefficients for the refractive index calculation of quartz crystals at room temperature 20° degrees Celsius [21].

| | **A** | **B** | **C** | **D** | **F** |
|---|---|---|---|---|---|
| $n_o$ | 1.28604141 | 1.07044083 | 1.00585997 | 1.10202242 | 100 |
| $n_e$ | 1.28851804 | 1.09509924 | 1.02101864 | 1.15662475 | 100 |

$$n^2_{\mathrm{o,e}} = A_{\mathrm{o,e}} + \frac{B_{\mathrm{o,e}}\lambda^2}{\lambda^2 - C_{\mathrm{o,e}}} + \frac{D_{\mathrm{o,e}}\lambda^2}{\lambda^2 - F_{\mathrm{o,e}}}, \tag{21}$$

$$\delta(\lambda) = d \times (n_e - n_o) \tag{22}$$

The calculation of the wavelength-dependent retardance follows equation 22. The refractive indices for the ordinary ray $n_0$ and extraordinary ray $n_e$ are calculated using equation 21 and the coefficients from table 2 [42][21].

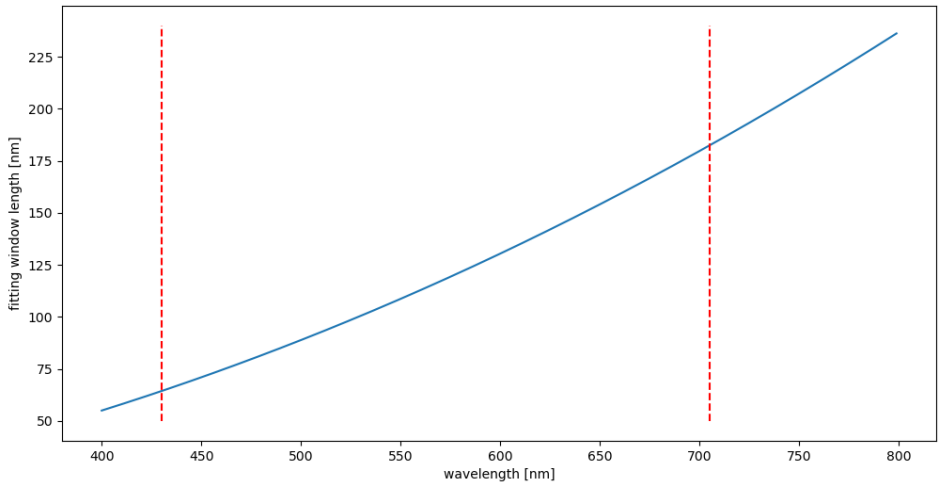


Figure 9: Fitting window length in nm with varying wavelength and cut-off wavelengths for a quartz crystals multiple-order retarder of thickness d = 0.3038145 mm.

The resulting fitting window length in nm is shown in Fig. 9. The two dotted red lines represent the cut-off wavelength and the lost polarization information at the spectrum edges. In a second step, the intensity spectrum $I_0(\lambda)$ for each measured data point is calculated by summing the modulated spectrum of both channels. The measured spectrum is then divided by the intensity spectrum $I_0(\lambda)$ to normalize the data.
In the following steps, the initial estimates for DoLP ($P_L$) and AoLP ($\phi$) are calculated. This is done, as well as the fit, for each spectral window. A first estimate for $P_L$ is derived by looking at the minimum and maximum data of the normalized measured intensity, as $P_L$ represents the amplitude of the oscillating cosine around 1/2. Afterwards, an artificial normalized reference signal is created using equation 15 or 16, $P_L = 1$, and $\phi = 0$.

For the initial $\phi$ estimate the cross-correlation of the measured normalized signal and the created normalized reference signal is calculated. A fit between the cross-correlation and $cos^2(\lambda + \lambda_\phi)$ is conducted to determine the shift $\lambda_\phi$. This shift is related to an initial estimate for $\phi$ by equation 23.

$$\phi_{estimate} = \frac{\pi \lambda_\phi}{\Delta\lambda(\lambda)} \tag{23}$$

Using the initial estimates for each spectral window and applying the boundaries $0 \leq \phi \leq \pi$ and $0 \leq P_L \leq 1$ the final fit of equation 15 or 16 in normalized form to the normalized measured spectrum is conducted.
The fit is conducted using sliding windows with the width of the local modulation periodicity for each measured data point. As the window width changes for each data point as explained before, the fit for $P_L$ and $\phi$ can experience artificial variations which are not reliable. Therefore, the results for $P_L$ and $\phi$ are smoothed by the width of the spectral windows. This results in the fact that the resolution for the polarization information is worse than the resolution of the spectrograph and depends on $\delta(\lambda)$ [42].

## 3.3 Data Processing

As described in chapter 2, the focus on GEO satellites comes with a reduced photon flux. Therefore, the raw measured data has to be processed in order to retrieve meaningful spectropolarimetric information.
The quality of measured data is usually defined as the signal-to-noise ratio (SNR). We assume that the noise is dominated by thermal or dark noise, photon noise, and quantization noise, which leads to the SNR definition shown by equation 24 for uncorrelated and random noise.

$$\frac{S}{N} = \frac{S}{\sqrt{N^2_{photon} + N^2_{dark} + N^2_{quantization}}} \tag{24}$$

We are going to improve the SNR by averaging in the spectral domain (pixel binning) and in the time domain (exposure stacking). For the following considerations, it is assumed that the noise components are uncorrelated, random, and have identical variance. This is of course a simplification, especially for the pixel binning.
The number of pixels or the wavelength range which can be used for binning without aliasing depends on the Nyquist pixel resolution, which is equal to $\frac{1}{2}$ the true spectrograph resolution dependent on the slit size and the grating. The SNR for the binning of n number of pixels will increase compared to the SNR of a single pixel according to equation 25 if the binning is conducted after the value read out. The SNR will improve by a factor of $\sqrt{n}$.

$$SNR_n = \frac{n \cdot S}{\sqrt{n} \cdot N} = \sqrt{n} \cdot SNR_{n=1} \tag{25}$$

Equation 25 holds as well for the signal averaging over multiple exposures in the time domain with n representing the number of exposures. The total SNR improvement is therefore reflected by equation 26. A pixel binning over 9 pixels and an averaging over 10 exposures would therefore improve the initial SNR by roughly 10.

$$SNR_{final} = \sqrt{n_{pixel}} \cdot \sqrt{n_{exposures}} \cdot SNR_{initial} \tag{26}$$

In a second step, the averaged exposure is corrected for the dark current by taking a dark exposure with matching integration time. Subsequently, the exposure is corrected for the sky background by subtracting a flat field image taken next to the desired target [29].

# 4 Instrumentation - The SSI

The following chapter describes the SSI as well as the other components needed for the satellite observations. First, an overview of all parts is given including an optical analysis of the SSI. Subsequently, the alignment procedure between the tracking camera and instrument is explained. Finally, the photon budget estimation for the SSI is analysed.

## 4.1 SSI Optical Train

Fig. 10 shows a schematic of the instrument optics mounted on the telescope. Table 3 depicts the corresponding part information. The overall instrumentation can be grouped into pre-instrument optics and the Spectropolarimter for Satellite Identification itself. The former comprises the telescope, a non-polarizing beamsplitter, and the tracking camera. The setup was chosen to simplify alignment between the optical origin of the tracking camera and the entry slit of the spectrograph, ensuring precise pointing and tracking of the chosen GEO satellite.

A Ritchey-Chrétien ASA AZ800 telescope owned by TNO is used for the observations. The $F/7$ system features two Nasmyth foci with an 80 mm access interface [2].
The telescope is followed by a non-polarizing beamsplitter with a reflection-transmission ratio of 10:90 and the ASI1600MM Pro tracking camera.
The first optical component of the SSI optical train, the collimating lens is an achromatic doublet from Thorlabs. The lens has an average reflectance of $R_{avg} < 0.5\%$ for the designed wavelength range of the AR coating [49]. The second optical component is an achromatic quarter-wave plate from Thorlabs. The average reflectance is again $R_{avg} < 0.5\%$[31]. The fast axis of the quarter-wave plate is aligned with the p-polarization axis and therefore with the transmitting direction of the polarizing beamsplitter and the following linear polarizer. The quarter-wave plate rotates the plane spanned by the Q/I,U/I Stokes vector components to the Q/I,V/I plane. The quarter-wave plate is followed by a multiple-order dual-wavelength retarder. The reflectance at the design wavelength is $R_{avg} < 0.25\%$. The retardance uncertainty is $< \frac{\lambda}{300}$. The wavelength-dependent retardance of the multiple-order retarder is calculated using the coefficients provided in table 2. The multiple-order retarder is not athermal, such that thermal errors might be present for the determined retardance [16]. The multiple-order retarder has its fast axis offset 45° degrees from the fast axis of the quarter-wave plate. It rotates the points in the Q/I,V/I plane around the U/I axis depending on the wavelength due to its chromatic nature. The multiple-order retarder is followed by a polarizing beamsplitter from Thorlabs. The beamsplitter has an overall average reflectance of $R_{avg} < 0.5\%$. The transmission for the passing light beam is $> 75\%$, and the reflectance for the redirected light beam is $> 70\%$ [54]. The polarizing beamsplitter finally projects all points onto the Q/I axis [42]. The final polarizing components are the linear wire-grid polarizers from Thorlabs, one having the optical axis parallel to the p-polarization direction and one parallel to the s-polarization direction. They have a transmission for the optical axis of $T_{avg} > 83\%$ [55]. The last optical components are the air-spaced Doublet collimators focusing the collimated beam into the optical fibre. Their alignment wavelength is 543 nm and their average reflectance is $R_{avg} < 0.5\%$. They focus the light into the optical fibres using a SMA adapter [1]. As optical fibres, 200 $\mu m$ multi-mode optical fibres are used. The spectrograph is the dual-channel fibre optics spectrograph AVASPEC-1650F-2-USB2. The detector is a Starline Sony2048 CCD [35][27].

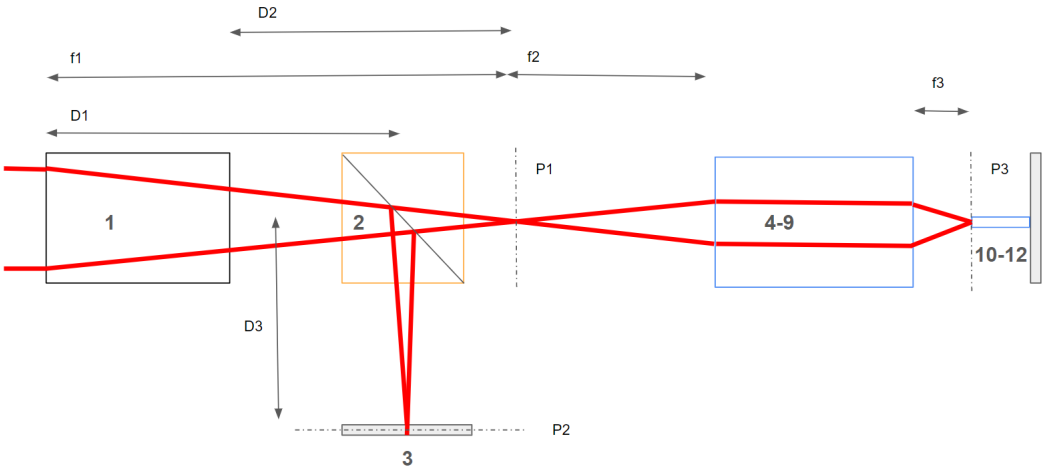


Figure 10: Schematic of the complete optical train. Part labelling 1-12 corresponds to Table 3. f1 = 5600 mm, f2 = 30 mm, f3 = 34.74 mm, D1 = 5442 mm, D2 = 258 mm, D3 = 158 mm P1/P2 = telescope focal plane, P3 = fiber collimating lens focal plane

Table 3: Sequence of optical parts used for observations with the SSI.
The part number corresponds to the labelling in Fig. 10.

| **Part Name** | **Part Number** | **Part Information** |
|---|---|---|
| Ritchey-Chrétien ASA AZ800 Telescope | 1 | aperture = 800 mm, focal length = 5600 mm<br>pointing accuracy $\leq$ 2 arcsec<br>Nasmyth focus |
| Non-Polarizing Beamsplitter | 2 | anti-reflection coating range = 400 - 700 nm<br>reflection-transmission ratio = 10:90 |
| ASI1600MM Pro Tracking Camera | 3 | sensor with 4656×3520 pixels, pixel size = 3.8 $\mu m$<br>angular field of view = 0.18° ×0.14 ° degrees |
| Achromatic Lens | 4 | anti-reflection coating range = 400 - 700 nm<br>focal length = 30 mm |
| Achromatic Quarter-Wave Retarder | 5 | anti-reflection coating range = 400 - 800 nm |
| Multiple-Order Retarder | 6 | dual anti-reflection coating at 532 nm and 1064 nm<br>quarter-wave plate at 532 nm<br>half-wave plate at 1064 nm<br>plate thickness = 0.3038145 mm<br>material = crystalline quartz |
| Polarizing Beamsplitter | 7 | anti-reflection coating range = 400 - 700 nm |
| 2 x Linear Polarizer | 8 | anti-reflection coating range = 420 - 700 nm |
| 2 x Fiber Collimating Lens | 9 | anti-reflection coating range = 350 - 700 nm<br>focal length = 34.74 mm |
| Multi-Mode Fibre | 10 | diameter = 200 $\mu m$, NA = 0.22 |
| AVASPEC-1650F-2-USB2 Spectrograph | 11 | blaze wavelength = 500 nm<br>grating = 300 l/mm for 450-900 nm<br>slit size = 200× 1000 $\mu m$<br>resolution = 9 nm |
| Starline Sony2048 CCD Detector | 12 | 1650 usable pixel, pixel size = 14×56 $\mu m$ |

## 4.2 Adapter

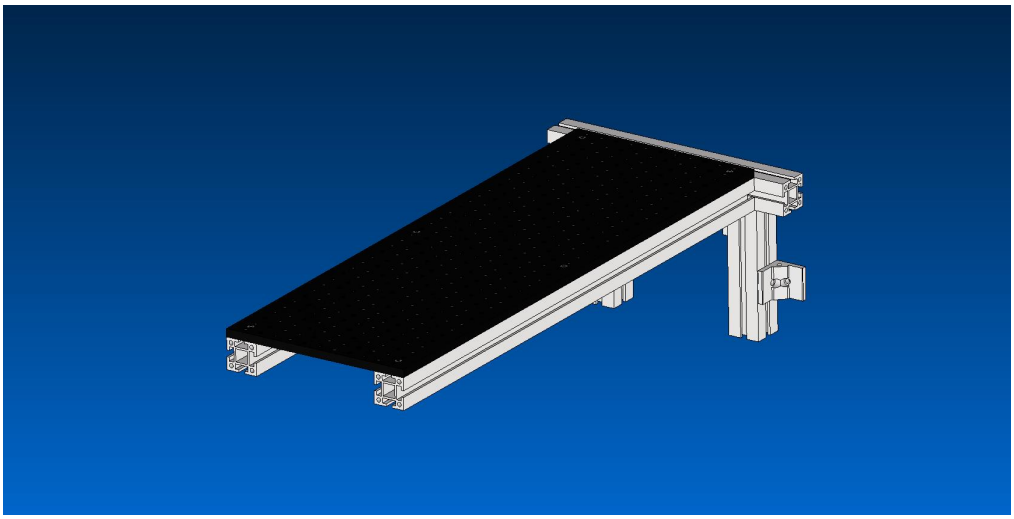

Figure 11: Telescope-Instrument adapter.

The adapter used to attach the instrument to the telescope is shown in Fig. 11. The instrument is arranged onto the breadboard and can be easily detached for the purpose of rearrangement. The adapter-breadboard arrangement is adjustable on all 3 axes in order to align the instrument with the optical axis and focus of the telescope.

## 4.3 Optical Analysis

The optical path through the telescope-instrument arrangement can be seen in Fig. 10.
The focal length f1 = 5600 mm is that of the telescope. The part that spans from the opening of the Nasmyth port to the focal point is given by D2 with 258 mm. The focal length of the collimating lens of the SSI is 30 mm and is denoted by f2. The non-polarizing beamsplitter is positioned at the distance D1 = 5442 mm from the M1 mirror of the telescope. To make the detector plane P2 of the camera coincide with the focal plane of the telescope the distance D3 therefore has to be 158 mm. The focal length of the fibre collimating lens of the SSI is f3 = 34.74 mm. The back focal plane of the telescope in the transmissive direction of the beamsplitter is named P1. P1 coincides with the front focal plane of the collimating lens of the SSI. The back focal plane of the SSI is P3 and is fed through the optical fibre to the spectrograph.
The formation of the image plane adheres to equation 27, where f is the focal length of the system, $s_1$ is the distance to the observed object, and $s_2$ is the distance to the image plane. Therefore, the image and the focal plane only coincide for objects at infinite distance and a detector placed in the focal plane usually experiences an unfocused image. To prevent this in the case of the SSI the focal length f1 of the telescope can be adjusted by moving the M2 mirror and therefore moving the focal plane and the image plane such that the image plane coincides with the detector plane of both the camera and the spectrograph. This ensures that the light is optimally focused on the optical fibre. If the SSI would be designed such that the detector plane always coincides with the focal plane (focal length not adjustable), the light would hit the detector with varying cone size based on the observation target and the angle of incidence would remain the same. This could lead to the optical fibre being overfilled and reduce the received photons at the spectrograph detector. However, a slightly larger spot size could also be beneficial if misalignment occurs and the multi-mode fibre is missed in the case of small spot size.

$$\frac{1}{f} = \frac{1}{s_1} + \frac{1}{s_2} \tag{27}$$

The diameter of the light beam at certain locations is also of interest to avoid vignetting.

The angle between the focal ray and the optical axis of the telescope is 4.09° degrees. The diameter of the beam at the Nasmyth focus opening is 36.90 mm. The diameter at the non-polarizing beamsplitter is 22.59 mm. The clear aperture of the non-polarizing beamsplitter is 22.9 mm. Therefore, no vignetting takes place in the case of perfect alignment. The collimated beam within the SSI is 4.29 mm in diameter. The clear aperture of the smallest component, the multiple-order retarder, is 10 mm.

## 4.4 SSI Field of View

Knowledge about the angular field of view (AFoV) is of importance for target pointing and tracking. The AFoV is given by equation 28. The detector of the tracking camera, which is in focus of the telescope, has a total width of 17.69 mm and a total height of 13.38 mm. This results in an AFoV of $0.18° \times 0.14°$ degrees.
For the SSI the AFoV of the slit is determined by three lenses compared to one for the camera. First, the collimated diameter from the $200\mu m$ fibre and collimation lens has to be determined. A good approximation of that is given by equation 29, where NA is the numerical aperture of the fibre and f is the focal length of the collimating lens. The used $200\mu m$ multi-mode fibre has a NA of 0.22 and the focal length is 34.74 mm. This results in a beam diameter of 15.28 mm. The beam diameter is shrunken to 10 mm by the vignetting of the clear aperture of the multiple-order retarder. This results in an AFoV for the SSI alone of 18.92° degrees. This has to be divided by the magnification ratio of the SSI collimating lens and the telescope focal length of $\frac{5600}{30} = 186.66$, which results in a total AFoV of 0.1 degrees. This is around $0.55 \times 0.70$ times the AFoV of the camera.

$$AFoV = 2 \cdot \arctan(\frac{h}{2f}) \tag{28}$$

$$D = 2 \cdot f \cdot NA \tag{29}$$

## 4.5 Alignment Procedure

The purpose of the alignment procedure is to ensure that the observation target tracked with the camera and telescope is positioned on the optical axis of the SSI such that the reflected flux of the target is received by the spectrograph. For that, the relative position between the SSI and the tracking camera has to be determined. Subsequently, the telescope has to be pointed such that the target appears in the optical centre of the SSI marked on the tracking camera detector, as determined beforehand.
A schematic of the first step of the alignment process is shown in Fig. 12. A light source is fibre-fed through the back of the SSI instrument. An additional collimating lens after the non-polarizing beamsplitter collimates the light and passes it to a retroreflector. For decent collimation, the light reflects back to the non-polarizing beamsplitter and is reflected to the detector of the tracking camera. The video mode of the camera software SharpCap can now be used with the minimum integration time of the camera of 32 $\mu s$ to adjust the relative position between the SSI instrument and the tracking camera. The projected spectrograph slit on the camera detector is brought into focus by adjusting the relative distance between the camera and the SSI optical train. The location of the focused spot can then be adjusted by a tip-tilt motion of the fibre collimating lenses or of the camera itself. The centre pixel of the projected slit is then marked using the SharpCap imaging software and taken as the optical origin of the spectrograph slit for the telescope pointing. This procedure has to be conducted for both spectrograph channels.

In the next step, the telescope is pointed to the target by feeding the respective TLE to the telescope tracking software. Offloading of the telescope in azimuth and elevation is then used to align the target visible on the tracking camera with the marked pixel position of the spectrograph slit.

The result is checked by taking an exposure and feeding it to a peak detection algorithm in Python based on a provided algorithm by TNO. The algorithm determines the peaks in the exposure, determines the pixel location of each, and fits a Gaussian profile to each peak found. An example is given in Fig. 13. The spot size in Fig. 13 is with 60-70 $\mu m$ larger than expected, as the exposure was saturated and by that, a larger sport size was fitted with the Gaussian fit. The pixel centre remains correct.

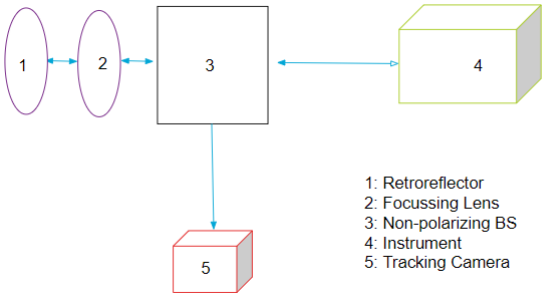


Figure 12: Schematic of laboratory alignment procedure between camera detector and spectrograph slit.

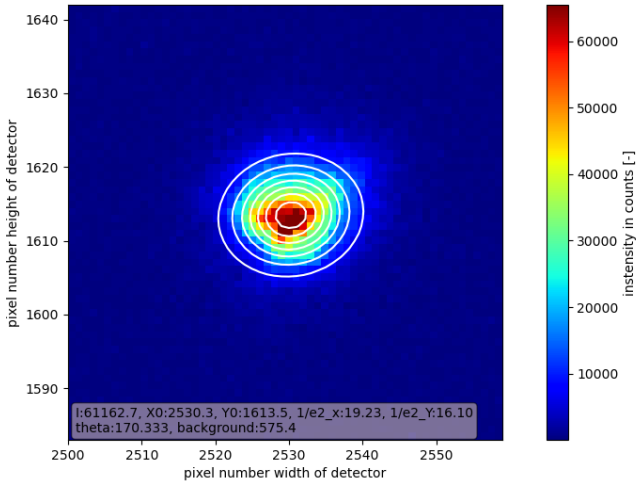


Figure 13: Observation of HD 10222 (Henry Draper catalogue) on 15.07.2022. Determination of pixel value for peak centre and spot size. $X_0 = 2530.3$, $Y_0 = 1613.5$, $1/e_x^2 = 19.23$, $1/e_y^2 = 16.10$.

## 4.6 Photon Budget Estimation

Estimating a photon budget prior to conducting the observations is crucial in order to tune the integration time and check for possible problems and misalignment.
The photon budget is estimated for the BVIR colour indices based on the Johnson-Morgan System to reflect the total wavelength range of the observations. The estimation framework is based on the work of Wijnen [53]. Additionally, the estimation is conducted for the p- and s-polarized channel with assumed DolP of 0.1, as they will have phase shifted amplitudes around the true intensity value of $\frac{1}{2}$DolP reducing the received flux per channel.

In the first step, the received amount of $\frac{\text{photons}}{\text{pixel} \cdot s}$ is calculated. The main input is the apparent magnitude of the target and the apparent magnitude of the sun -26.7.

The solar flux in $\frac{J}{s \cdot m^2 \cdot \mu m}$ is known for the desired wavelengths and we can use that to calculate the flux of the target by relating their apparent visual magnitudes. The flux in Joules is converted to photons by dividing it by Planck's constant times the speed of light in vacuum and multiplying it by the respective wavelength. Apparent magnitudes are usually defined on a $log_{10}$ scale given by equation 30. Taking the difference between the apparent magnitude of the target and that of the sun results in equation 31 solved for the flux of the target $F_x$. The flux is then multiplied by the spectral resolution of the spectrograph and the unobscured telescope aperture, and divided by the number of pixels per spectral resolution wavelength step. This yields the flux in $\frac{\text{photons}}{\text{pixel} \cdot s}$ at the top of the atmosphere.

$$m_x = -2.5 \cdot ln(\frac{F_x}{F_{x0}}) \tag{30}$$

$$F_x = F_S \frac{1}{10^{0.4 \cdot (m_x - m_S)}} \tag{31}$$

To estimate the true value received at the telescope one has to take into account the extinction of the atmosphere and correct the apparent magnitude according to equation 2. The average air mass for the GEO target satellites will be 2.5 according to equation 3 and figure 1a. Atmospheric extinction widely differs depending on wavelength, relative humidity, and aerosol content. For the sake of this rough estimation, the values given in table 4 [18] are used.

Table 4: Assumed atmospheric wavelength-dependent extinction values [18].

| **wavelength** | **atmospheric extinction value** |
|---|---|
| **B** | 0.4 |
| **V** | 0.2 |
| **R** | 0.1 |
| **I** | 0.08 |

The development of $\frac{\text{photons}}{\text{pixel} \cdot s}$ for a wavelength of 550 nm with varying apparent visual magnitude at the entrance of the telescope is depicted in Fig. 14 on a $log_{10}$ scale. It becomes clear, that the received flux decreases an order of magnitude when doubling the apparent visual magnitude. As discussed in section 2, the phase angle has a large influence on the received flux. The precise influence depends on the specific satellite, orbit, and time of observation. Based on the work of Bèdard et al. [10] and Zimmermann et al. [57] one can deduct knowledge about the overall influence. It is shown that for large phase angles there is no change in apparent visual magnitude to be expected. An exponential decrease in apparent visual magnitude can be observed for phase angles close to the minimum phase angle or glint. This phenomenon only occurs for a small phase angle range $< 10°$ degrees close to the minimum phase angle. However, Bèdard et al. [10] showed that the apparent visual magnitude can decrease from 14 to 2 close to the minimum phase angle. In order to incorporate the phase angle influence, it is recommended to take photometric observations of each target satellite and deduce a relationship for the minimum phase angle range. If the satellite is not observed close to the minimum phase angle it can be assumed that the phase angle does not have an influence on the received flux. Otherwise, it aids the observations as more photons are received.

In the next step, the optical throughput of the whole instrument is estimated to calculate the received flux at the detector pixel. An overview of all assumed values can be found in table 6. If there are two values given, the first value represents the one for the p-polarization channel and the second for the s-polarization channel.

The development of $\frac{\text{photons}}{\text{pixel} \cdot s}$ for a wavelength of 550 nm with varying apparent visual magnitude at the detector after applying the total estimated throughput and the quantum efficiency is depicted in Fig. 15 on a $log_{10}$ scale. The estimated flux can be used to check the instrument alignment and validate the photon budget model.

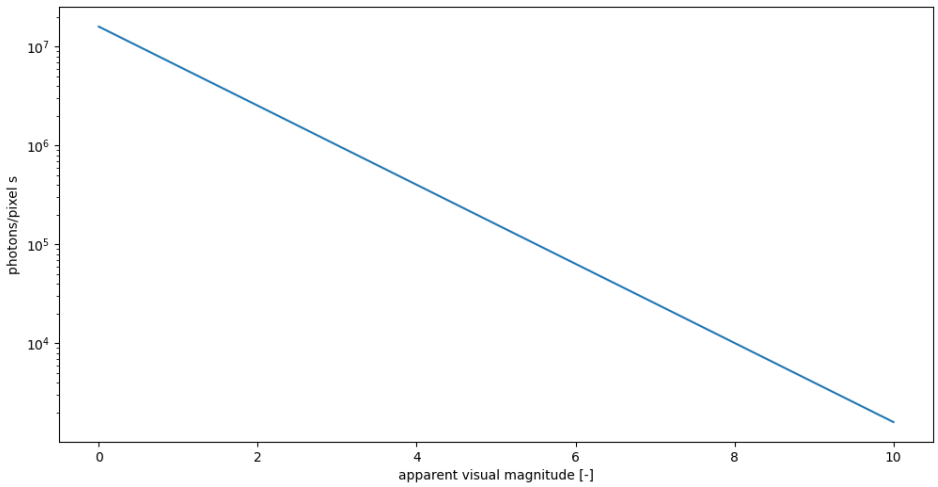


Figure 14: Received photons/pixel second with varying apparent visual magnitude for the wavelength of 550 nm at the entrance of the telescope.

Table 5: Assumed wavelength-dependent values for the optical throughput of each SSI component [1][16][31][49][54][27][35].

| Component | B | V | R | I |
|---|---|---|---|---|
| Non-Polarizing Beamsplitter | 0.8 | 0.8 | 0.8 | 0.8 |
| Collimating Lens | 0.97 | 0.97 | 0.97 | 0.97 |
| Fiber Collimator Lens | 0.98 | 0.98 | 0.98 | 0.98 |
| Quarter-Waveplate | 0.95 | 0.955 | 0.96 | 0.955 |
| Multiple-Order Retarder | 0.98 | 0.99 | 0.99 | 0.98 |
| Beamsplitter | 0.75/0.70 | 0.75/0.70 | 0.75/0.70 | 0.75/0.70 |
| Wiregrid Polarizer | 0.9 | 0.9 | 0.9 | .09 |
| Optical Fiber | 0.79 | 0.83 | 0.85 | 0.86 |
| Spectrograph | 0.52 | 0.48 | 0.39 | 0.26 |
| Total Throughput | 0.17/0.14 | 0.17/0.14 | 0.14/0.12 | 0.09/0.08 |
| Detector Quantum Efficiency | 0.24 | 0.4 | 0.27 | 0.08 |

Table 6: Instrument Optical Throughput

Based on the desired SNR ratio a needed integration time can now be estimated taking into account the main noise components. The main noise components, photon noise, dark noise, and quantization noise and their influence on the SNR are shown in equation 32 [29].

$$
\begin{aligned}
N &= \sqrt{S_{phot}(QE)t_{imt} + S_{dark}t_{imt} + N^2_{quantization}} \\
\frac{S_{\text{detected}}}{N} &= \frac{(S_{phot})\,(QE)\,(t_{int})}{\sqrt{S_{phot}(QE)t_{int} + S_{dark}t_{int} + N^2_{quantization}}} \\
\frac{S_{\text{detected}}}{N} &= \frac{(S_{phot})\,(QE)\,(t_{int})}{\sqrt{t_{imt}\left[S_{phot}(QE) + S_{dark}\right] + N^2_{quantization}}}
\end{aligned}
\tag{32}
$$

$$
0 = t^2_{int} - t_{int}\frac{\frac{S}{N}^2 S_{phot}QE + \frac{S}{N}^2 S_{dark}}{(S_{phot}QE)^2} - \frac{\frac{S}{N}^2 N^2_{quantization}}{(S_{phot}QE)^2} \tag{33}
$$

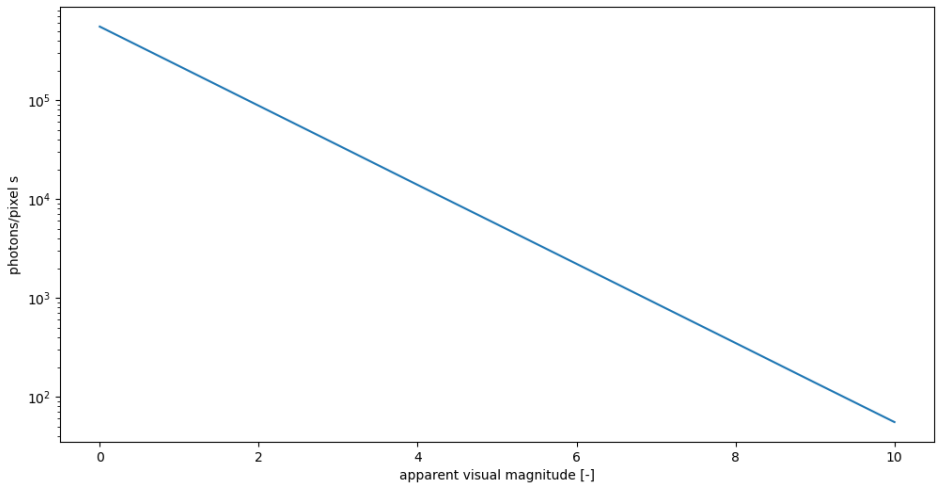


Figure 15: Received photons/pixel second with varying apparent visual magnitude for the wavelength of 550 nm at the detector.

The equation for SNR can be rearranged as given by equation 33 to calculate the needed integration time for the corresponding noise level. To get a sound estimation the dark current noise and baseline noise have to be known. Therefore, we conducted dark current measurements in the laboratory. We took measurements over a range of integration times from 1.05 ms to 40 s. By performing a linear fit we are able to determine the time-dependent dark current noise and the static baseline or quantization noise. We took 100 exposures per integration time step. The mean values over the visual wavelength are depicted in Fig. 16a. It becomes obvious that both channels experience high dark noise and baseline noise. As we are going to correct each observation by a dark current measurement taken beforehand, the standard deviation of the dark current measurements is the true noise component. Nevertheless, knowledge about the uncorrected dark current noise is important, as the well depth of the detector is only 40,000 counts which leads to saturation for higher integration times. Those values are given in Fig. 16b. It can be seen that the measurements do not follow a linear fit anymore for higher integration times. The reason for that could be saturated pixels, hot pixels, or another unknown characteristic of the detector. For the purpose of this thesis, the values estimated by the fit are multiplied a safety factor of 2 and used for the integration time estimation.

The estimated integration time for an SNR of 10 varying with apparent visual magnitude and wavelength is depicted in Fig. 17 on a $log_{10}$ scale. The needed integration time roughly increases an order of magnitude by doubling the apparent visual magnitude. It becomes clear, that the system loses efficiency at the edges of the spectrum, especially on the red side. This can be mainly attributed to the throughput of the spectrograph and quantum efficiency of the detector. For a higher efficiency over the whole wavelength range, a more suited spectrograph should be considered. The needed integration time for an apparent visual magnitude of 10, the expected value for a GEO satellite, is estimated to be $10^2$ s for the red end of the spectrum and $10^1$ s for wavelength values around 550 nm. The effect of the phase angle is not considered here. For higher required SNR the needed integration time would further increase. However, the SNR can also be improved by pixel binning and image stacking as discussed in section 3. Overall it is therefore expected that if the estimated photon budget is correct, it is possible to observe GEO satellites using the SSI, especially when conducted close to the minimum phase angle.

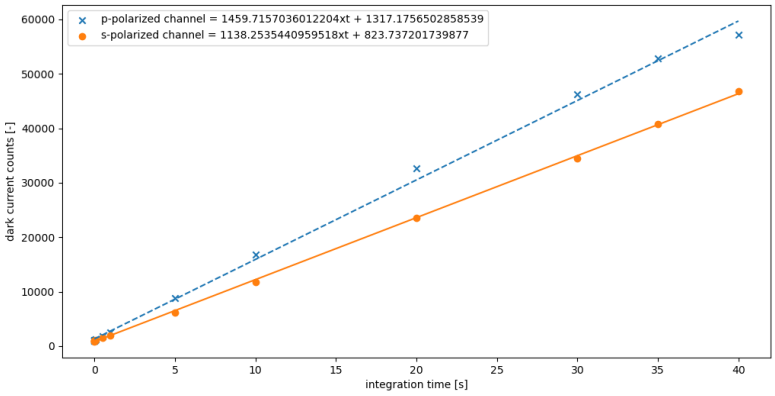


(a)

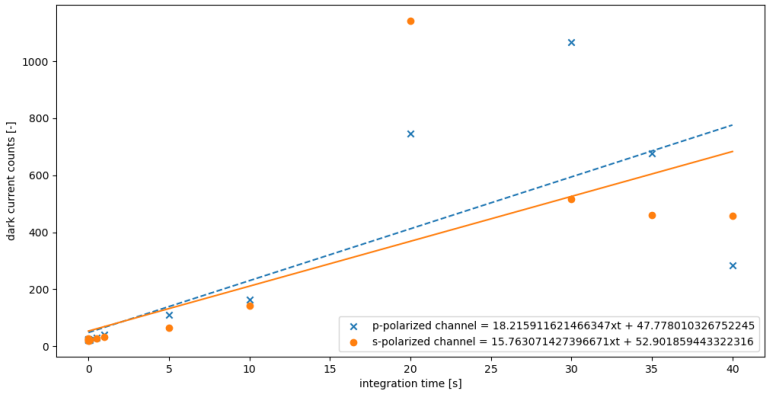


(b)

Figure 16: Dark current estimation for the Starline Sony2048 CCD Detector in a laboratory environment at 25° degrees Celcius. (a) shows the mean value over 100 exposures. (b) shows the standard deviation over 100 exposures.

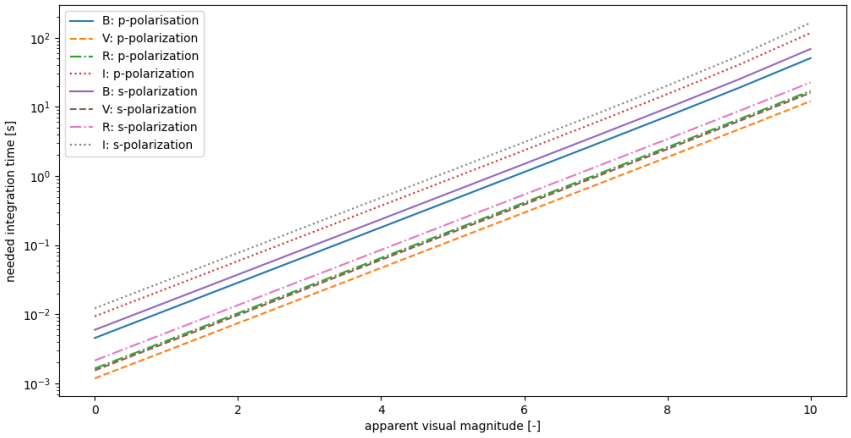


Figure 17: Estimated needed integration time for a SNR of 10 with varying apparent visual magnitude and wavelength for the p- and s-polarized channel on a $log_{10}$ scale.

# 5 Laboratory Testing, Verification and Validation

Chapter 5 summarizes the software verification, the laboratory testing and calibration, and concludes with an analysis of the laboratory validation.

## 5.1 Software Verification

In order to conduct a sound analysis of the observation results the used algorithms have to be verified. The software verification is conducted for the retrieval algorithm of the linear polarization information as well as for the iterative transmission correction. Verification is conducted by feeding simulated input with known output to the algorithm and comparing the outcome to the expected values.

### 5.1.1 Retrieval Algorithm Verification

The simulated input for the verification is depicted in Fig. 18a. We used three different input signals, DolP = 0 and AolP = 0° degrees, DolP = 1 and AolP = 0° degrees, and DolP = 0.45 and AolP = 31.72° degrees. The expected and retrieved values for DolP and AolP are shown in Fig. 18b and 18c respectively. It becomes clear that the algorithm is able to retrieve the linear polarization information with high precision in the simulated case. The existing residuals due to the fit are minimal and can be neglected. Therefore, the retrieval algorithm is verified.

### 5.1.2 Transmission Correction Algorithm Verification

The transmission correction algorithm was tested using four different cases in order to simulate the most challenging cases. For every simulation, the simulated input, the true and estimated transmission difference, as well as the true and estimated DolP, are plotted. Additionally, the RMS error is calculated and summarized in table 7. Every simulation used 10 iterations of the algorithm.
Simulation I was conducted for no transmission difference and 0 DolP. The results are depicted in Fig. 19b and 19c. Simulation II was conducted for no transmission difference and 0.5 DolP. The results are depicted in Fig. 20b and 20c. The iterative transmission correction does not induce an error for both cases and the RMS error values are negligible.
Simulation III was conducted for a linear decreasing transmission difference and a DolP of 0. The results are depicted in Fig. 21b and 21c. The algorithm does reproduce the correct transmission difference quite accurately with a sinusoidal error pattern. This error pattern is due to the fit used in the algorithm. The RMS error values for the transmission difference of 0.002 and DolP of 0.003 are acceptable.
Simulation IV was conducted for a totally random transmission difference and DolP of 0. The results are depicted in Fig. 22b and 22c. Again, the algorithm is able to estimate the true transmission difference quite precisely. The DolP RMS error of 0.01 would pose a problem if sub 1% accuracy is needed for the observations. For the purpose of this proof of concept, the error margin is excepted. Especially, as the introduced transmission correction algorithm achieves way better results and accuracy than formerly used algorithms for the modulation pattern at hand. Therefore, the transmission correction algorithm is verified.

Table 7: RMS error values for the transmission correction algorithm verification.

| | **Simulation I** | **Simulation II** | **Simulation III** | **Simulation IV** |
|---|---|---|---|---|
| **Transmission RMS** | 3.19E-14 | 8.65E-11 | 0.002 | 0.004 |
| **DolP RMS** | 4.71E-5 | 1.44E-9 | 0.003 | 0.01 |

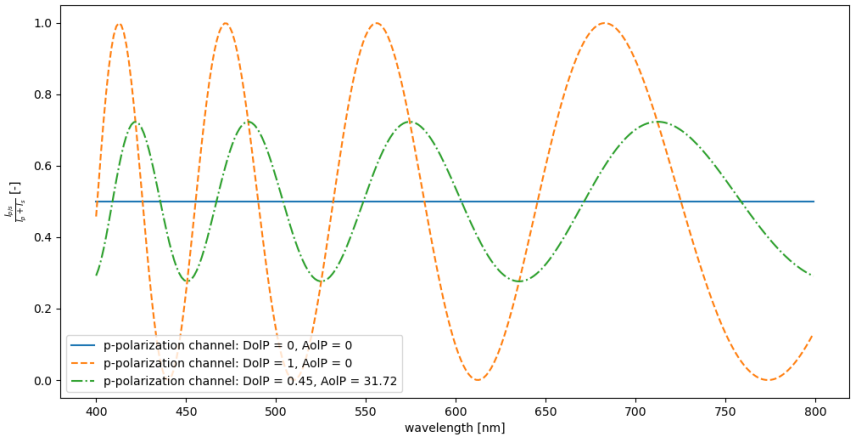


(a)

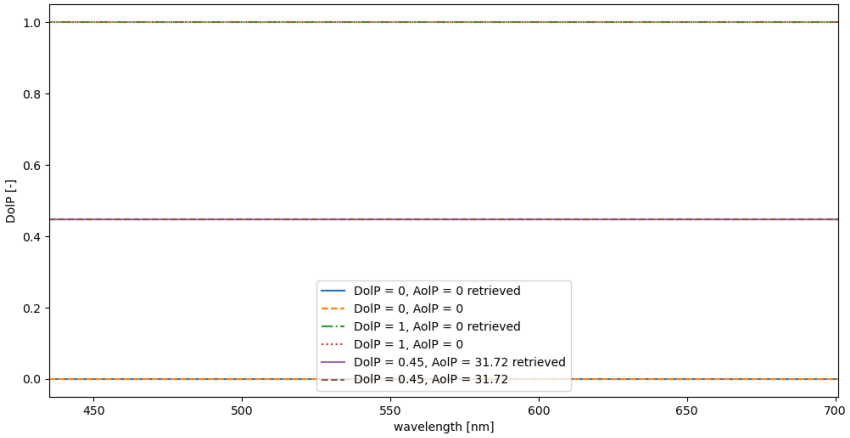


(b)

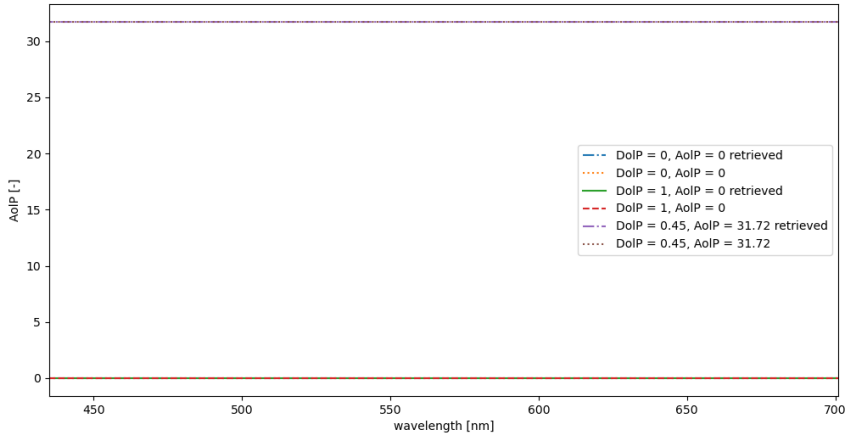


(c)

Figure 18: Verification of retrieval algorithm. (a) simulated input. (b) retrieved and expected DolP. (c) retrieved and expected AolP.

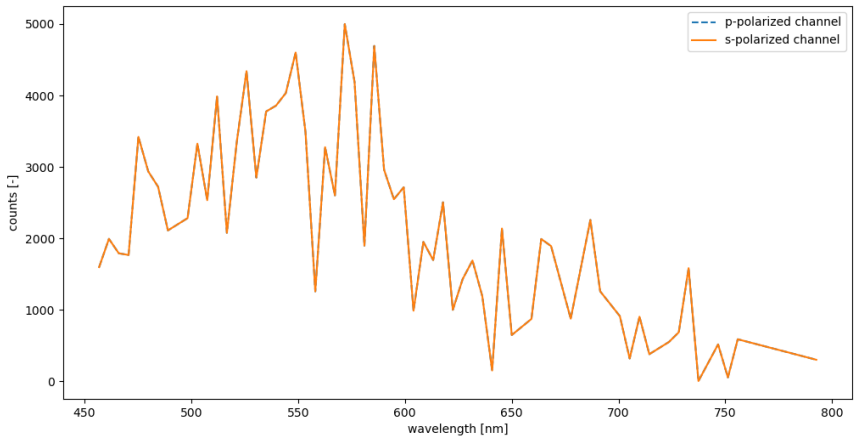


(a)

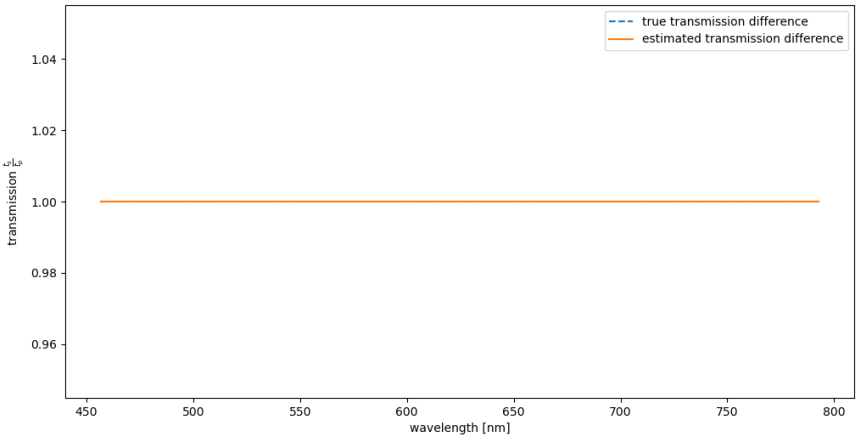


(b)

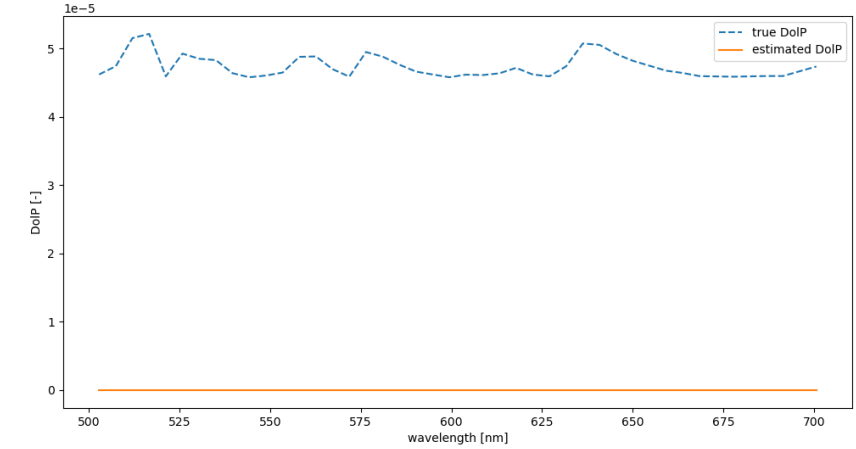


(c)

Figure 19: Verification of transmission correction algorithm. (a) simulated input of no transmission difference and 0 DolP. (b) true and estimated transmission. (c) true and estimated DolP.

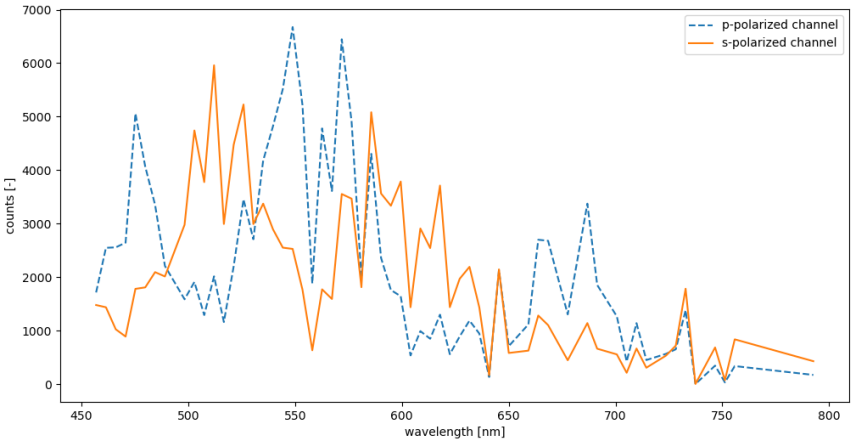


(a)

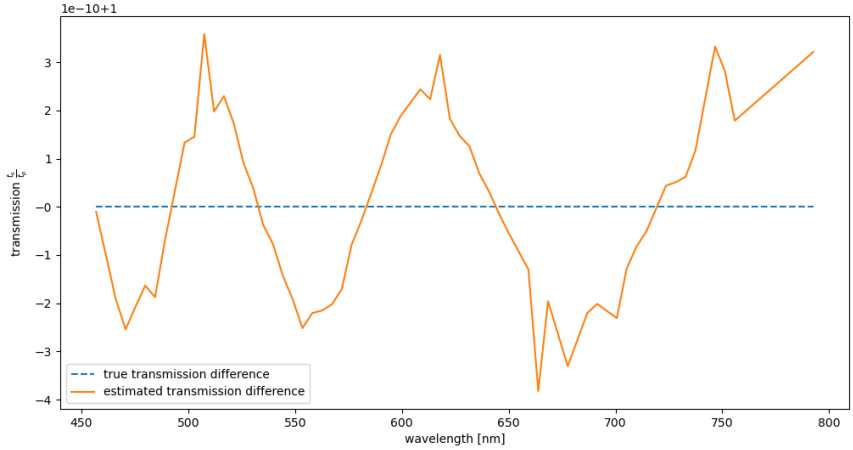


(b)

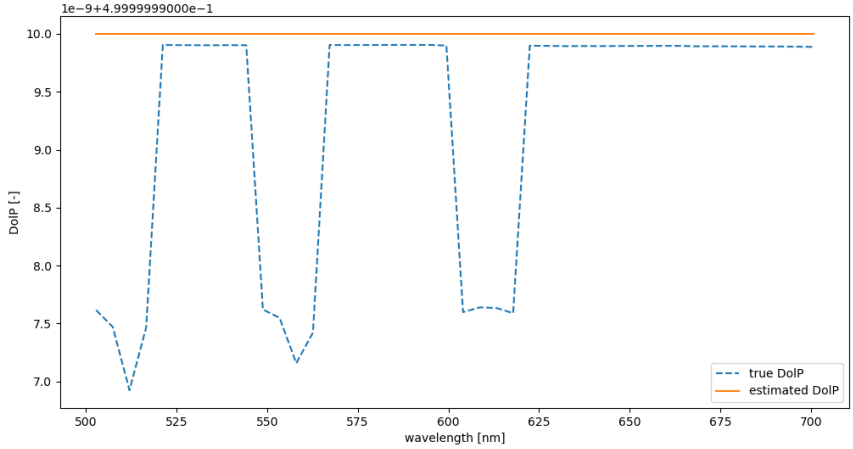


(c)

Figure 20: Verification of transmission correction algorithm.(a) simulated input of no transmission difference and 0.5 DolP. (b) true and estimated transmission. (c) true and estimated DolP.

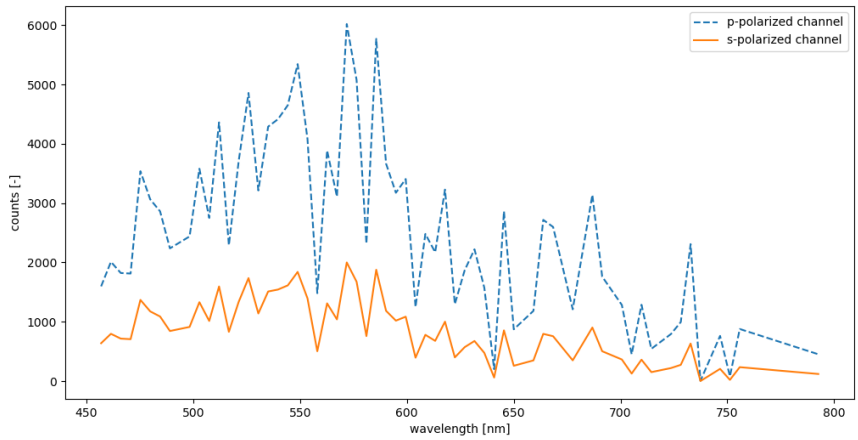


(a)

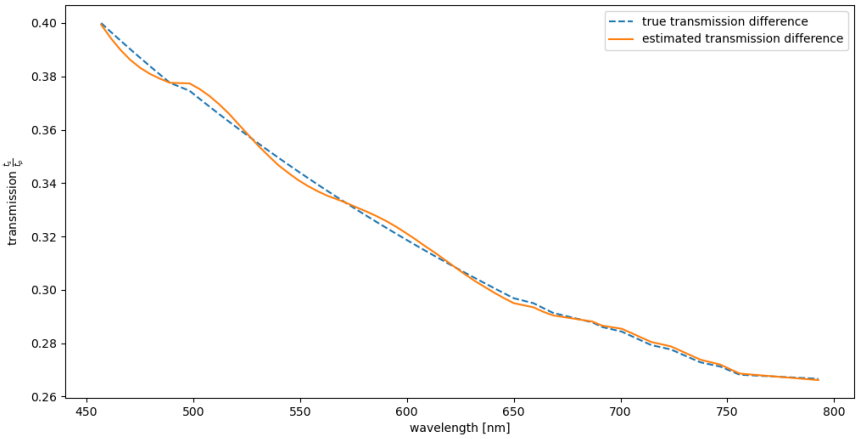


(b)

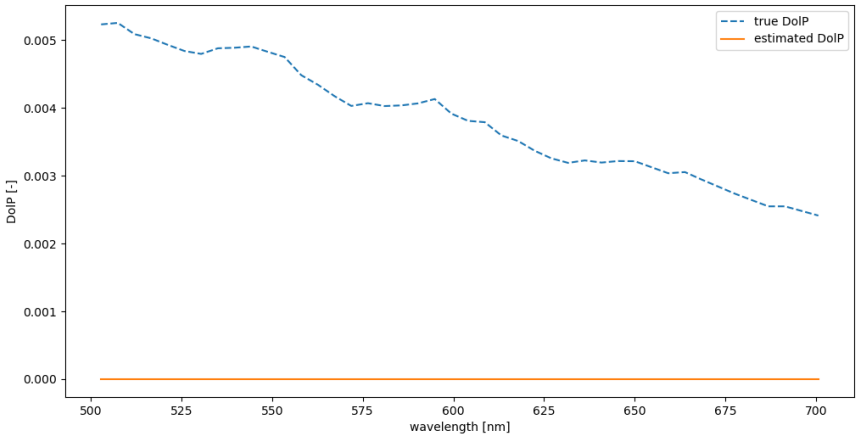


(c)

Figure 21: Verification of transmission correction algorithm.(a) simulated input of linear decreasing transmission difference and 0 DoLP. (b) true and estimated transmission. (c) true and estimated DoLP.

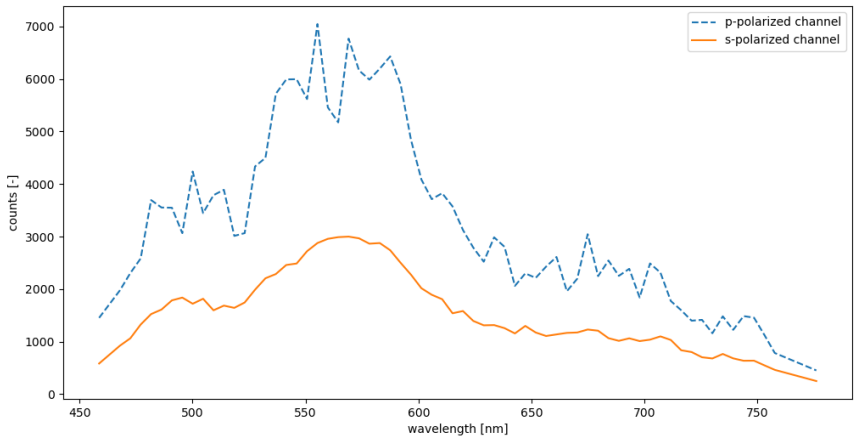


(a)

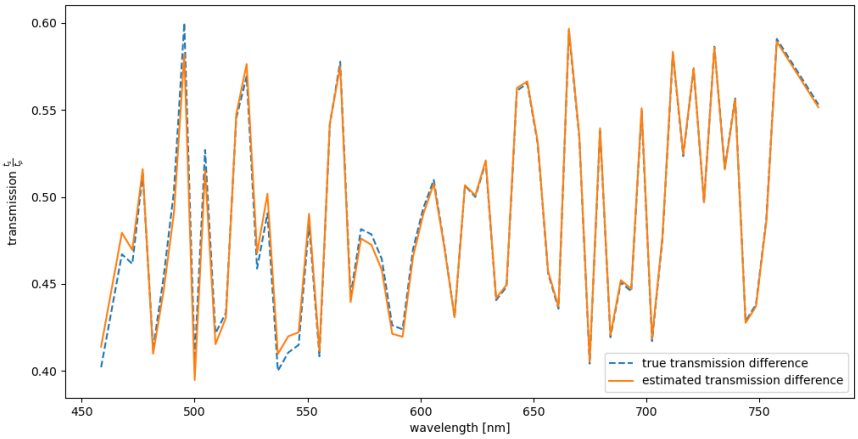


(b)

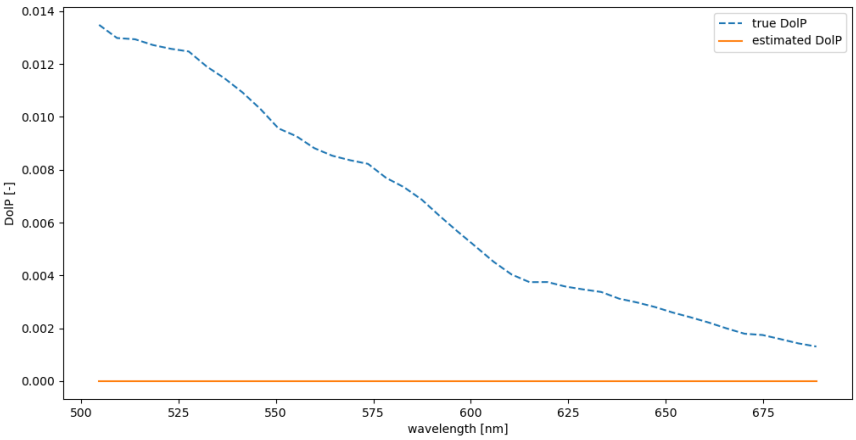


(c)

Figure 22: Verification of transmission correction algorithm. (a) simulated input of random transmission difference and 0 DolP. (b) true and estimated transmission. (c) true and estimated DolP.

## 5.2 Static Error Analysis

There is a multitude of errors that can distort the retrieved linear polarization information. As static errors we define the error components that we can calibrate for and such should not falsify the retrieved linear polarization information after a sound calibration.

### Slit Function

The slit function or instrument response function represents the spectral resolving ability of the used spectrograph. If the modulated signal has spectral features with a smaller resolution than the spectrograph the features will not be resolved correctly. The convolution of the slit function and the modulated signal will then result in a smearing of the modulation. This is especially true for shorter wavelengths, as the local modulation period is shorter. An example is depicted in Fig. 23. The reduced modulation amplitude and smearing of the spectrum are clearly visible around 400-500 nm. The reduction of modulation amplitude is quite strong [41].

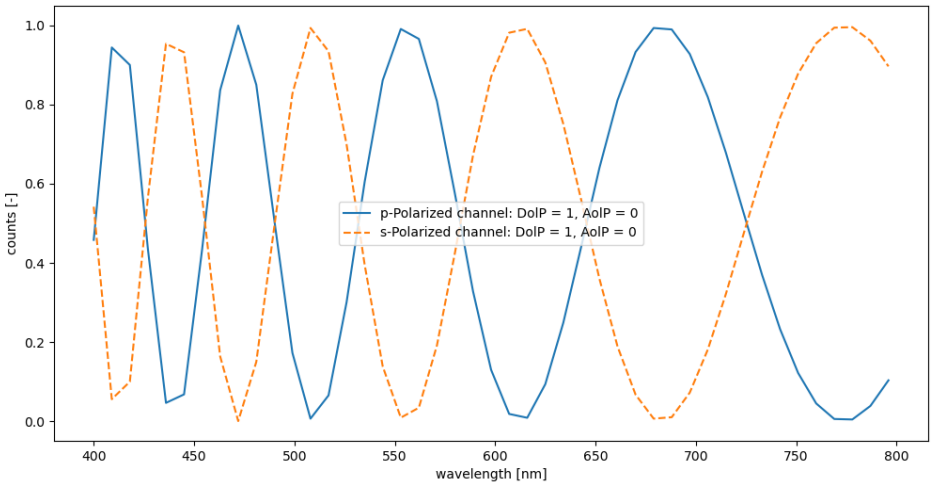


Figure 23: Simulation of slit function effect. Simulated with DoLP = 1, AoLP = 0° degrees, and spectral resolution of 9 nm.

### Retardance Error

The true retardance of the quarter-wave plate and the multiple-order retarder can differ from the expected theoretical value. This will lead to a different modulation equation reducing the modulation amplitude. In the case of the multiple-order retarder, this also leads to an error in the retrieved AoLP and DoLP. The retrieval algorithm uses theoretical values for the retardance. An offset leads to a shift in retrieved AoLP and by that an induced error in DoLP. Fig. 24 depicts the reduction in modulation amplitude for a retardance error of the quarter-wave plate of 15%. It is clear, that the reduction for such a large error is quite small. Additionally, the effect depends on the Stokes vector of the incoming signal. Therefore, the error will not be prominent in the overall modulation efficiency [25].

### Alignment Error

The theoretical modulation equation only holds for a precise alignment of the components. An alignment error in the quarter-wave plate and multiple-order retarder will induce additional sinusoidal terms which cause a phase shift. Alignment errors of the polarizing beamsplitter and linear polarizers will reduce the modulation amplitude. A misalignment of the quarter-wave plate of 2° degrees is depicted in Fig. 25. The induced phase shift is clearly visible, already for a small alignment error of 2° degrees. We expect to observe the error in the calibration activities [25].

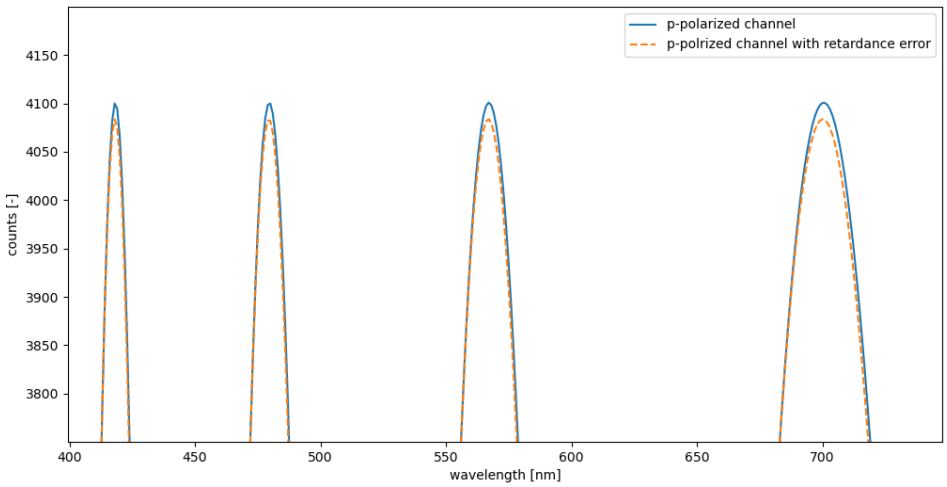


Figure 24: Simulation of quarter-wave plate retardance error of 15%.

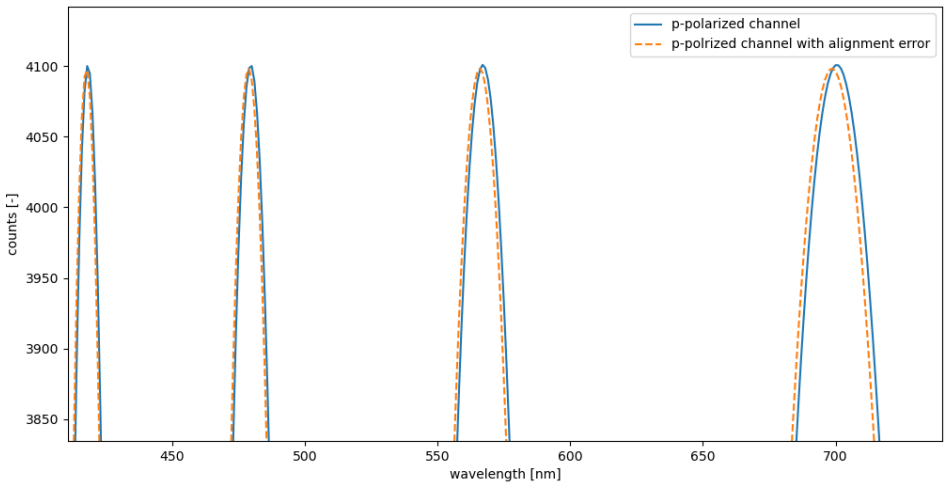


Figure 25: Simulation of quarter-wave plate alignment error of 2° degrees.

### Diattenuation Error

The quarter-wave plate and the multiple order retarder feature birefringent material. Birefringent material has a refractive index depending on the orientation of the light. This feature is used to induce retardance on the incoming signal. As the transmission through the material is governed by the refractive index, birefringent material will induce a slight polarization according to the Fresnel equations. For the quarter-wave plate, this will lead to an additional instrument-induced polarization modulated by the multiple-order retarder. For the multiple-order retarder, the modulation amplitude is going to be reduced.

### Non-normal Incidence Error

The same effect as for the diattenuation error is amplified for non-normal incidence according to the Fresnel equations. Additionally, non-normal incidence changes the applied retardance of the quarter-wave plate and the multiple-order retarder.

The quarter-wave plate will therefore reduce the modulation amplitude and the multiple-order retarder will induce a phase error. Additionally, the non-normal incidence would also cause induced polarization by the collimating lens and by that reducing the modulation amplitude.

**Instrument Induced Polarization Error**

The above described instrument-induced polarization has been mainly due to the quarter-wave plate and the multiple order retarder. Those errors can be eliminated by laboratory calibration. However, a large part of the instrument-induced polarization is caused by the non-polarizing beamsplitter and the telescope itself. Unfortunately, there has been no opportunity to take extensive calibration measurements using the telescope and non-polarizing beamsplitter due to time constraints. Therefore, at this point, we give a theoretical overview of the expected induced polarization. It is recommended to conduct the calibration measurements when the time allows for it.

The used non-polarizing beamsplitter features a reflection-transmission ratio of 10:90. The difference for the transmission between the p- and s-polarized component of the incident light beam $T_p - T - s$ is $< 10\%$. Therefore, the beamsplitter could induce polarization and by that alter the retrieved DolP and AolP up to the error value of $< 10\%$ [34].
The used azimuth-elevation telescope features a Nasmyth port. The purpose of the M3 folding mirror is to reflect the gathered light to the Nasmyth port for different azimuth-elevation combinations. It follows, that the M3 mirror experiences a changing reflection angle. Induced polarization and phase shift by mirrored surfaces are not as problematic as for glass optics. Especially the induced polarization effect of symmetric mirrored surfaces is minimum and can be neglected. Therefore, the M1 and M2 mirrors of the used telescope are assumed to not induce any polarization or phase change [44][46]. However, as the M3 mirror is not symmetric, it will induce polarization and a phase change. The reflected light of a surface is governed by the general Fresnel equations combined with Snells law given by equation 34 [7]. The refractive index $n_1$ of air can be assumed to be 1. The refractive complex index of the material is $n_2 = n + ik$, where n is the refraction index and k absorption coefficient.

$$\begin{aligned} R_s &= \left| \frac{n_1 \cos\theta_\mathrm{i} - n_2 \sqrt{1 - \left(\frac{n_1}{n_2}\sin\theta_\mathrm{i}\right)^2}}{n_1 \cos\theta_\mathrm{i} + n_2 \sqrt{1 - \left(\frac{n_1}{n_2}\sin\theta_\mathrm{i}\right)^2}} \right|^2 \\ R_p &= \left| \frac{n_1 \sqrt{1 - \left(\frac{n_1}{n_2}\sin\theta_\mathrm{i}\right)^2} - n_2 \cos\theta_\mathrm{i}}{n_1 \sqrt{1 - \left(\frac{n_1}{n_2}\sin\theta_\mathrm{i}\right)^2} + n_2 \cos\theta_\mathrm{i}} \right|^2 \end{aligned} \tag{34}$$

An induced polarization as a difference between the p- and s-polarized component as well as a phase change will therefore depend on the angle of incidence $\theta_i$. The Mueller matrix for the M3 mirror can then be set up according to equation 35, where $R_s$, $R_p$, and $\Delta$ are all dependent on the angle of incidence $\theta_i$ [22]. This can be used to calculate the true incident Stokes vector using Mueller calculus.

$$M_{M3} = \frac{1}{2} \begin{bmatrix} \mathrm{R}_s + R_p & \mathrm{R}_s - Rr_p & 0 & 0 \\ \mathrm{R}_s - R_p & \mathrm{R}_s + R_p & 0 & 0 \\ 0 & 0 & 2\sqrt{\mathrm{R}_s R_p}\cos\Delta & 2\sqrt{\mathrm{R}_s R_s}\sin\Delta \\ 0 & 0 & -2\sqrt{\mathrm{R}_s R_s}\sin\Delta & 2\sqrt{\mathrm{R}_s R_p}\cos\Delta \end{bmatrix} \tag{35}$$

Giro et al. showed that one can expect up to a 4 % induced increase for the Q ad U Stokes vector components [22]. Therefore, the telescope and non-polarizing beamsplitter induced error is relatively high and has to be corrected for and further investigated.

## 5.3 Dynamic Error Analysis

Dynamic errors can occur due to changing environmental factors. Due to their volatile nature one can not calibrate for them.

### Temperature Effects

The used multiple-order retarder is not athermal. Therefore, there is going to be a temperature-induced error. The material of multiple-order retarders, in our case crystalline quartz, is quite temperature sensitive. The material will change its refractive indices depending on the present temperature and by that change the induced retardance. That will lead to a phase shift in the modulated spectrum and an error in retrieved AolP, which affects the retrieved DolP in second order [42].
There are several options to deal with the induced error. The most sophisticated one would be to produce an athermal multiple-order retarder by crossing two multiple-order wave plates. Another approach would be to treat the induced retardance of the multiple order retarder as a variable in the wavelength window fit. That would be an easier method than creating the athermal multiple-order retarder, but the resulting fit would suffer, as an extra variable is introduced. For this proof of concept, it was decided to derive temperature coefficients for the refractive indices of crystalline quartz and correct the former calculated values for a temperature difference from 20° degrees Celsius room temperature. The true refractive index is calculated using equation 36. Based on the work of Toyoda et. al [48] we derived the wavelength-dependent temperature coefficients for the ordinary and extraordinary refractive index for a wavelength range between 500-800 nm shown in table 8.

$$n_T = n_{T_0} + \frac{dn}{dT} \times \Delta T \tag{36}$$

Table 8: Wavelength-dependent temperature coefficients for the refractive indices of crystalline quartz in $\frac{10^{-6}}{K}$

| $\frac{dn}{dT}$ | **500 nm** | **600 nm** | **700 nm** | **800 nm** |
|---|---|---|---|---|
| $n_0$ | -6 | -6.5 | -7 | -7.5 |
| $n_e$ | -7 | -8 | -8.5 | -9 |

### Non-Normal Incidence

Non-normal incidence can also occur as a dynamic error. The effects are the same as described above. This might especially be the case for unprecise target tracking.

### SNR Effects

The SNR can also have an effect on the retrieved polarization information. A low SNR can extinguish low DolP as the modulation pattern might not be detectable anymore. A SNR of 10 corresponds to a possible signal offset of 10%. Looking at the modulation equation 18, this corresponds to a DolP of 0.1. If the random signal offset occurs over the full modulation period, the cosine pattern will not be detectable anymore. The exact effect can not be quantified due to the nature of the fit and the random noise, but SNR should be as high as possible if the other observation parameters can be satisfied.

## 5.4 Calibration

The modulation equations 15 and 16 represent the theoretical relations without errors. Those errors can be summarized in an efficiency term $W(\lambda)$ as shown in equation 37 [41]. The polarimetric efficiency is mainly dominated by the slit function or instrument response function, more prominent in the short wavelength region due to the higher modulation frequency. Other main contributing errors amongst others are misalignment, retardance offset and temperature effects [42].

$$\begin{aligned} \langle I_p \rangle (\lambda) &= \frac{1}{2} I_0(\lambda) \left\{ 1 + W(\lambda) \left( q \cos\left(\frac{2\pi\delta}{\lambda}\right) - u \sin\left(\frac{2\pi\delta}{\lambda}\right) \right) \right\} \\ \langle I_s \rangle (\lambda) &= \frac{1}{2} I_0(\lambda) \left\{ 1 - W(\lambda) \left( q \cos\left(\frac{2\pi\delta}{\lambda}\right) - u \sin\left(\frac{2\pi\delta}{\lambda}\right) \right) \right\} \end{aligned} \tag{37}$$

Laboratory calibration was done using a laser-driven light source in combination with an integrating sphere to ensure a non-polarized input signal. Wavelength calibration was conducted using a Mercury-Argon spectral line lamp. After the laboratory calibration campaign, we performed validation measurements using a double glass plate setup to induce low levels of DoLP. We will not conduct radiometric calibration as this is beyond the scope of this thesis and is not needed for the proof of concept.

### Wavelength Calibration

To infer a possible wavelength drift of the used dual-channel spectrograph we fitted a Gaussian distribution to the detected peaks and compared the estimated mean to the reference values for each spectral line.
The absolute difference for both channels to the indicated spectral lines is given by Fig. 26. The maximum drift is smaller than 2.8 nm and therefore around one-third of the spectral resolution. Nevertheless, we updated the coefficients of the polynomial to convert pixel values to a unit of wavelength by fitting a fourth-order polynomial through the usable spectral lines for both channels separately. The old and updated coefficients of the polynomial given by equation 38 are summarized in table 9.

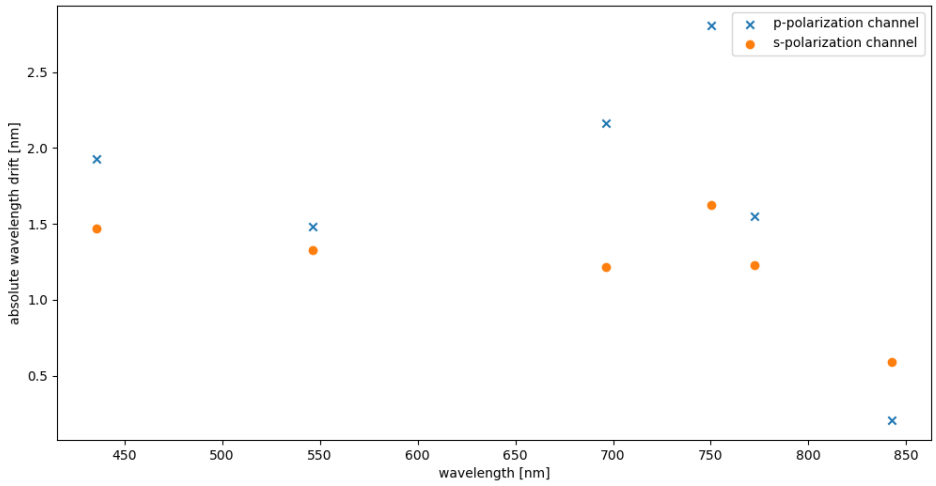


Figure 26: Absolute wavelength drift of used dual-channel spectrograph with respect to reference Mercury-Argon spectral line lamp.

$$\lambda = C_1 + C_2 \times pixnr + C_3 \times pixnr^2 + C_4 \times pixnr^3 + C_5 \times pixnr^4 \tag{38}$$

Table 9: Old and updated coefficients for the 4th order polynomial to convert pixel value to wavelength [nm] for both channels.

| coefficients | p-pol. old | p-pol. updated | s-pol. old | s-pol. updated |
|---|---|---|---|---|
| **c1** | 4.0413006E+2 | 402.131 | 4.10337E+2 | 408.341 |
| **c2** | 5.994051E-1 | 0.600941 | 5.923698E-1 | 0.598602 |
| **c3** | -2.0419836E-5 | 1.1581E-05 | -1.461097E-5 | -3.78507E-05 |
| **c4** | -5.1348619E-10 | -1.40237E-07 | -3.428349E-9 | 3.0693E-08 |
| **c5** | 0 | 1.33751E-10 | 0 | -1.50677E-11 |

The absolute difference to the true reference values of the Mercury-Argon line lamp after updating the coefficient is depicted in Fig. 27. The maximum wavelength difference is $< 0.8$ nm.

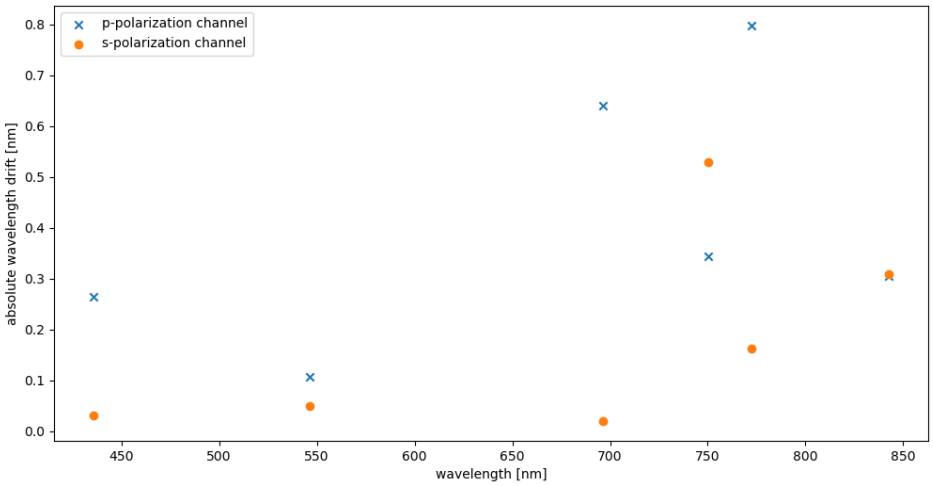


Figure 27: Absolute wavelength drift of used dual-channel spectrograph with respect to reference Mercury-Argon spectral line lamp after update of the coefficients.

### Polarimetric Calibration

In a first step, a measurement of the unpolarized input signal is taken to analyse if the instrument itself induces a polarization signal which has to be corrected for. Fig. 28 shows the normalized difference between the p- and s-polarization channels given by equation 19. After transmission correction, a possible polarized signal would be a cosine centred around 0 with an amplitude equal to the DolP. Therefore, Fig. 28 indicates that there is no measurable induced polarization by the instrument itself. The remaining deviation from 0 is due to the applied iterative transmission correction.

For the determination of the polarimetric efficiency, a linear polarizer is used to 100% polarize the input signal. A generalized form of the normalized measured count given by equation 37 is depicted by equation 39 for the s-polarized channel, where $\beta$ is the input AoIP. This indicates, that the measured output for an input signal modified by a linear polarizer turned over 360° degrees undergoes a double period variation. An example is depicted in Fig. 29 for a wavelength of 500 nm. Equation 40 is therefore fitted to the measured signal for each wavelength point in order to estimate the coefficients M1, M2, and M3. Equations 41 and 42 are then used to calculate the polarimetric efficiency. The procedure is repeated for the p-polarized channel [41].

$$\frac{I_s(\lambda)}{I_0(\lambda)} = \frac{1}{2} t(\lambda)_s \left\{1 + \cos 2\beta m_{S,q} + \sin 2\beta m_{S,u}\right\} \tag{39}$$

$$f_{\text{fit}}\ (\beta) = M_1 + \cos 2\beta M_2 + \sin 2\beta M_3 \tag{40}$$

$$m_{S,q} = \frac{M_2}{M_1}; \quad m_{S,u} = \frac{M_3}{M_1} \tag{41}$$

$$W_S(\lambda) = \sqrt{\left(m_{S,q}(\lambda)\right)^2 + \left(m_{S,u}(\lambda)\right)^2} \tag{42}$$

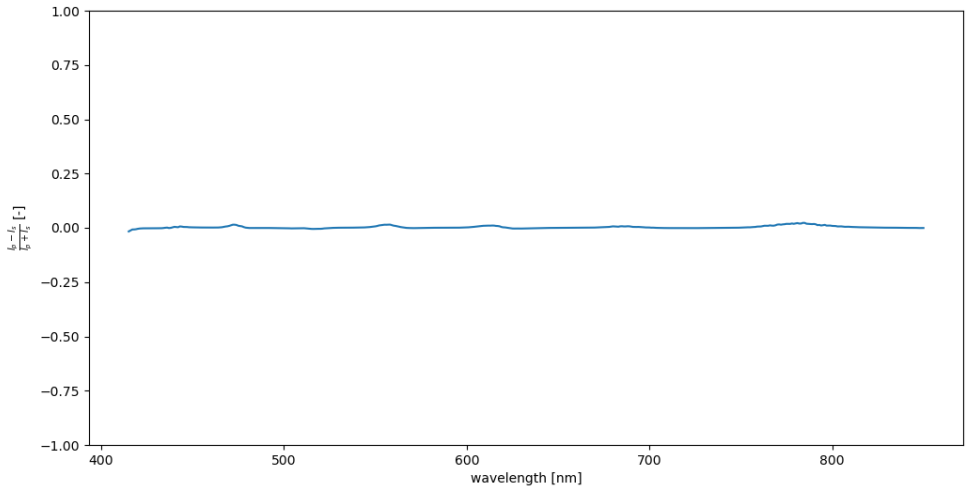


Figure 28: Normalized difference between p- and s-polarization channel for an unpolarized input signal.

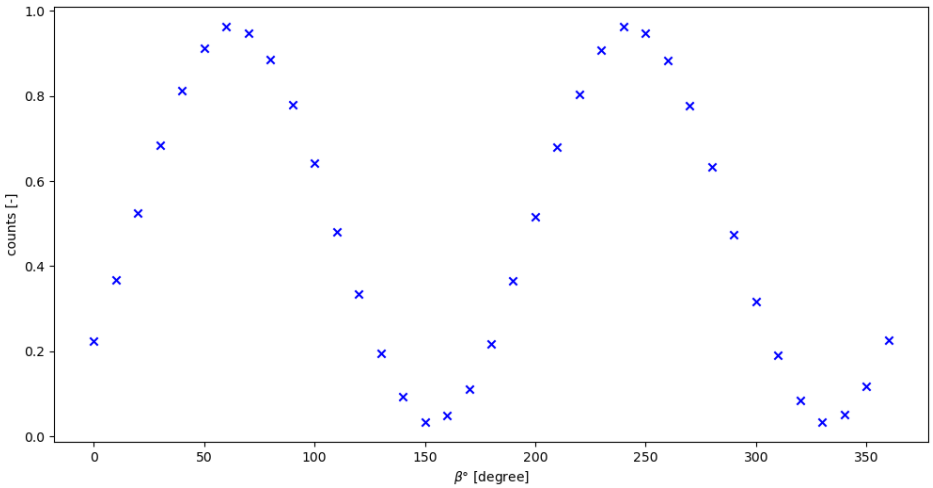


Figure 29: Double period variation for a wavelength of 500 nm and a varying input angle of linear polarization $\beta$.

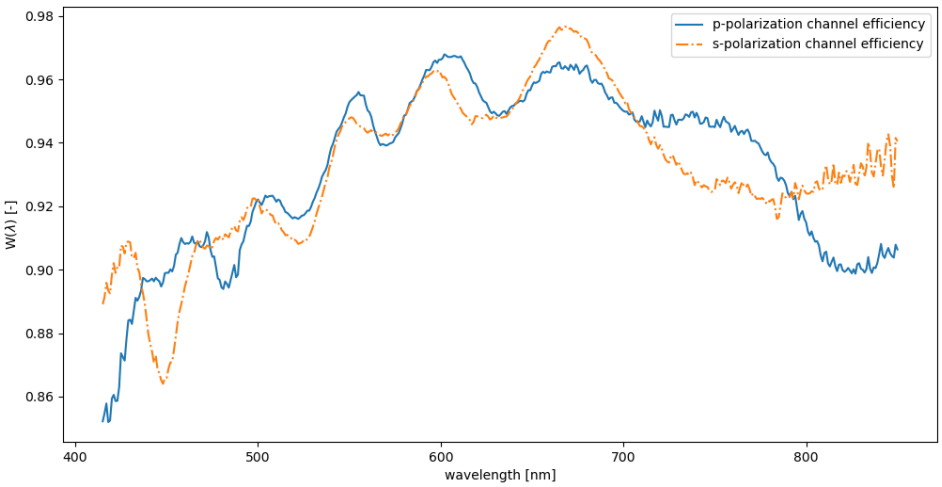


Figure 30: Polarimetric efficiency for p- and s-polarization channel.

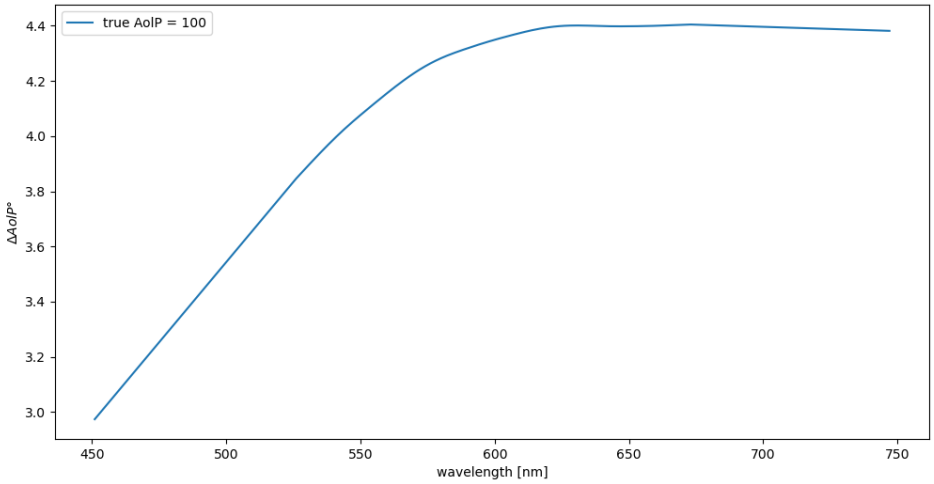


Figure 31: Offset between retrieved and true AolP for a true AolP of 100° degrees.

The resulting efficiency for the p- and s-polarization channel is shown in Fig. 30.
The polarimetric efficiency is not equal for both channels. The modulation pattern is mainly caused by a misalignment of the components introducing small sinusoidal terms as can be expected for an off-the-shelf setup. As explained above, the alignment error introduces a phase shift and by that also an error for the retrieved DolP. That would also explain the main difference in efficiency between the p- and polarized channels. This is also confirmed by Fig. 31. Fig. 31 depicts the offset between retrieved and true AolP for a true AolP of 100° degrees. The same holds for the whole range of AolP. The maximum observed offset is 5.6° degrees. The relative lower efficiency for the blue side of the spectrum reflects the influence of the slit function. The reduced efficiency at the red end of the spectrum could be caused by the range of the anti-reflection coatings of the optical components. An example of the effect of the polarimetric calibration is shown in Fig. 32. It is clearly visible that the applied efficiency correction pushes the modulation amplitude up to the true value of 1.

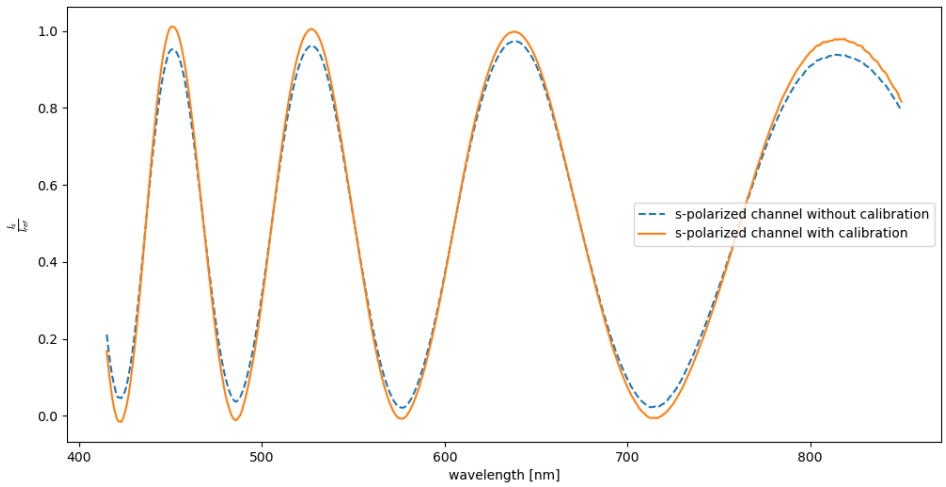


Figure 32: S-polarized channel for a DolP of 1 with and without calibration applied.

## 5.5 Validation

The induced polarization by the double glass plate setup was calculated by using the Fresnel equations depicted by equation 34 and the wavelength-dependent refractive indices for the used BK7 glass depicted in table 10. The glass plates were turned in opposite directions to eliminate the induced shift of the light beam. The glass plate mount can be turned in steps of 5° degrees. An example for the induced and retrieved DolP for a glass plate angle of 45° degrees is shown in Fig 33a.
The retrieved and theoretical values of DolP for a glass plate angle ranging from 20° - 60° degrees are shown in Fig. 33b. The absolute error between calculated and retrieved values is depicted in Fig. 33c. The SSI seems to be able to reproduce the theoretical values with an accuracy $\leq 1.2$ % DolP, more accurate for higher values of induced DolP. The validation of sensitivity was limited by the angle resolution of the glass plate setup. Nevertheless, it was shown that the SSI is able to distinguish DolP signals $\geq 1.3$ % in a laboratory environment.

Table 10: Used wavelength-dependent refractive index for BK7 glass [38].

| $\lambda$ [nm] | n | $\lambda$ [nm] | n | $\lambda$ [nm] | n | $\lambda$ [nm] | n |
|---|---|---|---|---|---|---|---|
| 410 | 1.5296 | 432 | 1.5271 | 454 | 1.5249 | 476 | 1.5231 |
| 498 | 1.5215 | 520 | 1.5201 | 542 | 1.5189 | 564 | 1.5178 |
| 586 | 1.5168 | 608 | 1.5159 | 630 | 1.5151 | 652 | 1.5144 |
| 674 | 1.5137 | 696 | 1.5131 | 718 | 1.5125 | 740 | 1.5120 |
| 762 | 1.5115 | 784 | 1.5111 | 806 | 1.5106 | 828 | 1.5102 |

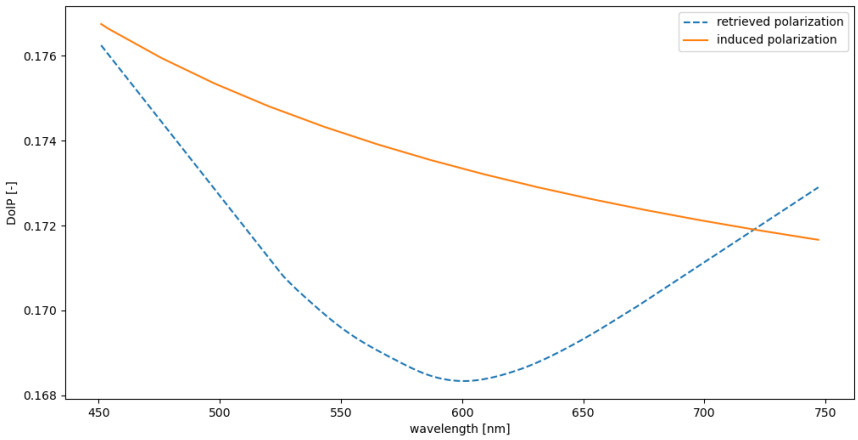


(a)

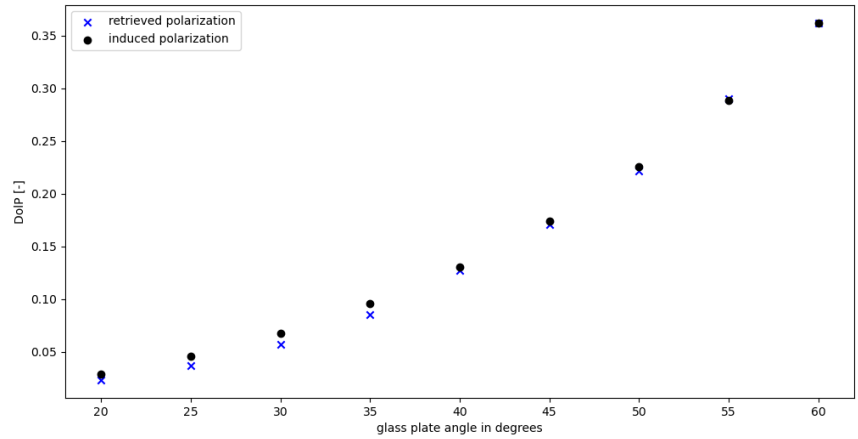


(b)

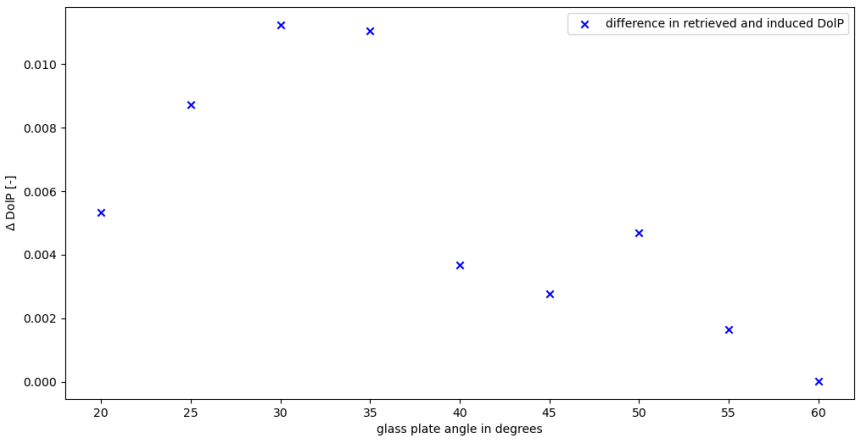


(c)

Figure 33: Results of the validation measurements using a double glass plate setup. (b) example measurement for a glass plate angle of 45° degrees. (b) mean of the retrieved and induced DoIP. (c) absolute error between retrieved and induced DoIP.

# 6 Preliminary Observations

This chapter summarizes the preliminary observations conducted with the SSI at the TNO owned Ritchey-Chrétien ASA AZ800 telescope at The Hague. Due to time constraints and problems with the alignment procedure we were only able to conduct preliminary observations of bright stars.

## 6.1 Observation of Arcturus - HD 124897

HD[1] 124897 was observed on the night of 14.07.2022. We used an integration time of 30 ms and averaged the measured spectrum over 100 exposures. The spectrum after the subtraction of the dark noise is depicted in Fig. 34a. The general signal level is quite low and one can observe a large transmission difference between the p- and s-polarized channels. One can also observe a few negative values after dark noise subtraction for the s-polarized channel. HD 124897 has an apparent visual magnitude close to 0. Based on the photon budget we would expect a maximum received count value of 16,000. We observe a maximum count value of around 5% of that with 800 counts. This could be a hint that the system experienced a misalignment and had a reduced photon throughput. This would also confirm the large transmission difference between both channels, as this was not observed in the laboratory beforehand.
The spectrum after pixel binning and removing outliers is depicted in Fig. 34b. The corrected spectrum after application of the iterative transmission correction is shown in Fig. 34c. It is clear that for a large range of the spectrum there is no difference between both channels. A slight modulation is only visible between 450 and 550 nm. This is also confirmed in the retrieved DolP given by Fig. 37a. We retrieved a linear decreasing DolP of 2.5% at 500 nm to 1% at 575 nm. Afterwards, the retrieved DolP is negligible. The expected linear polarization of HD 124897 is too low to be detected by the SSI [3]. Nevertheless, we would expect to see the in chapter 5 described induced polarization by the telescope and instrument. The DolP found for HD 124897 in the wavelength range between 500-575 nm is in the expected range of the induced polarization by the M3 mirror of the telescope [22]. The drop-off towards the longer wavelengths can not be explained at the moment. However, as the induced polarization of the M3 and the non-polarizing beamsplitter are wavelength dependent, one would expect a noticeable difference. Nevertheless, one should be cautious as the retrieved DolP could also be an artefact of the iterative transmission correction. However, this seems unlikely, as the found values are above the determined laboratory accuracy of $\leq$ 1.2 % DolP. As shown during the algorithm verification, this accuracy is mainly determined by the iterative transmission correction.

## 6.2 Observation of Polaris - HD 8890 and HD 10307

We observed HD 8890 and HD 10307 on the night of 14-15.07.2022. HD 8890 was observed with an integration time of 400 ms and HD 10307 of 7 s. We only took one exposure. HD 8890 has an apparent visual magnitude of around 2, and HD 10307 of around 5. For both stars the measured spectrum after dark noise subtraction is given by Fig. 35a and Fig. 36a. We can clearly observe a hot pixel and a broken pixel after dark current subtraction. For HD 10307 the spectrum also rather looks like a top hat function compared to the other measurements. It can also be observed that the transmission difference between both channels is not as strong anymore. This could be another hint that the system experienced misalignment, as the light beam probably enters the system now at a different angle which leads to a transmission difference due to the sensitivity of the fibre collimating lenses. For HD 8890 and HD 10307 we would expect a maximum count value of 35,000 and 38,000. Again, the actual received count is around 5% of the expected value. This steady offset over all 3 observations can either be attributed to a misalignment of the instrument or a model error of the photon budget estimation. We believe that there has been an issue with the alignment procedure, as this was also confirmed by subsequent failed observation attempts. The retrieved DolP for HD 8890 and HD 10307 is given by Fig. 37b and 37c respectively. All retrieved values are below the laboratory-determined accuracy value.

[1] Henry Draper catalogue

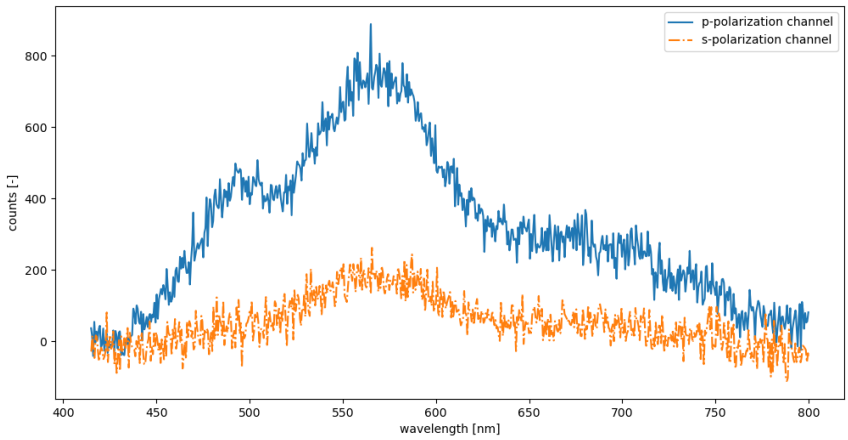


(a)

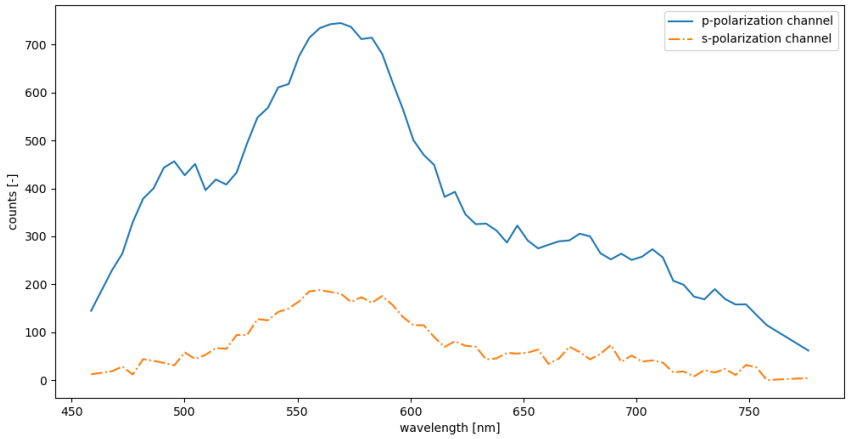


(b)

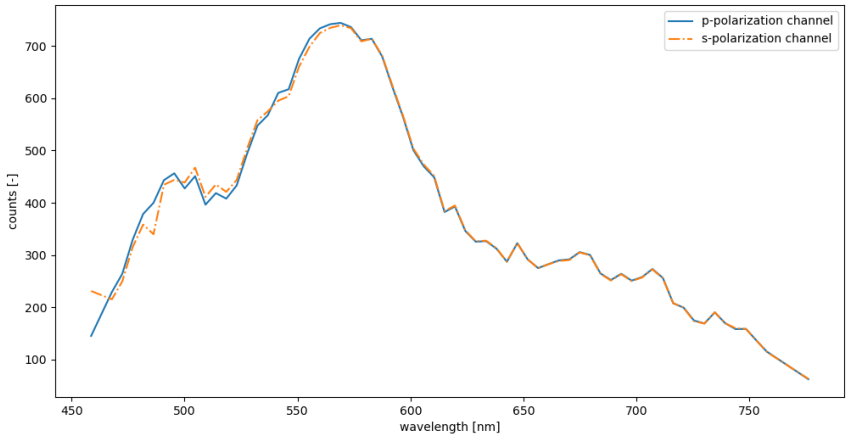


(c)

Figure 34: Observed spectrum of HD 124897 on the night of 14.07.2022. (a) shows the spectrum after dark current correction. (b) depicts the spectrum after pixel binning. (c) the final spectrum after applying the iterative transmission correction.

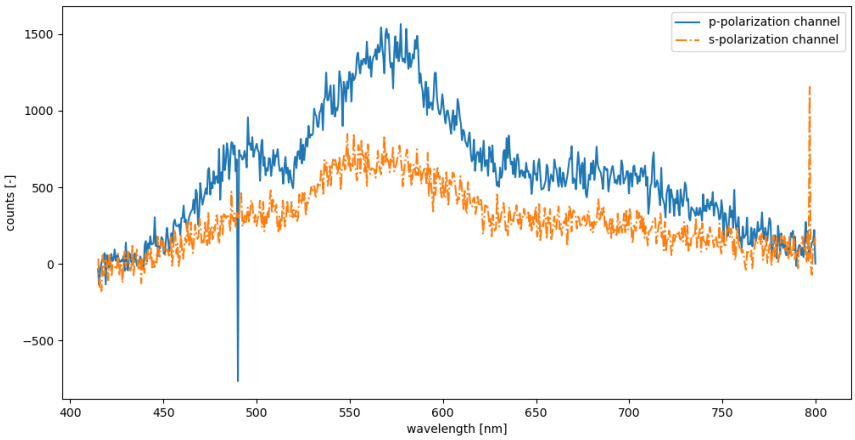


(a)

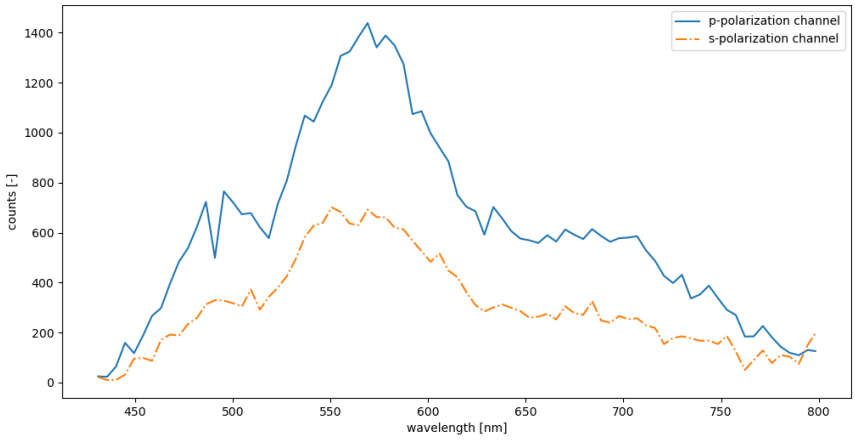


(b)

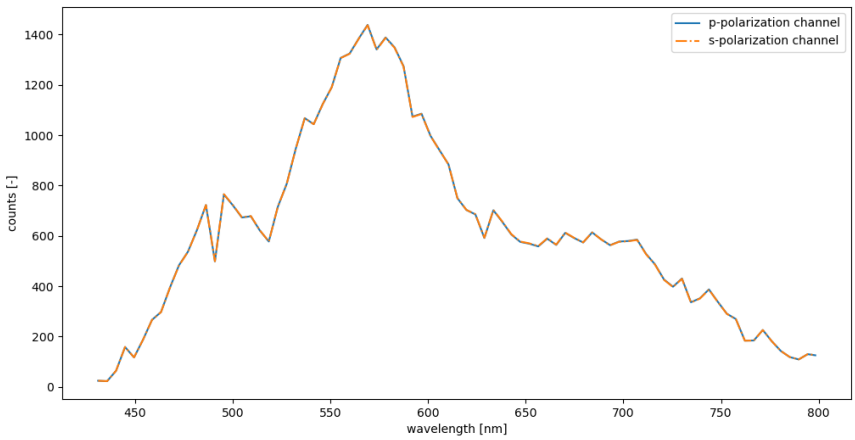


(c)

Figure 35: Observed spectrum of HD 8890 on the night of 14.07.2022. (a) shows the spectrum after dark current correction. (b) depicts the spectrum after pixel binning. (c) the final spectrum after applying the iterative transmission correction.

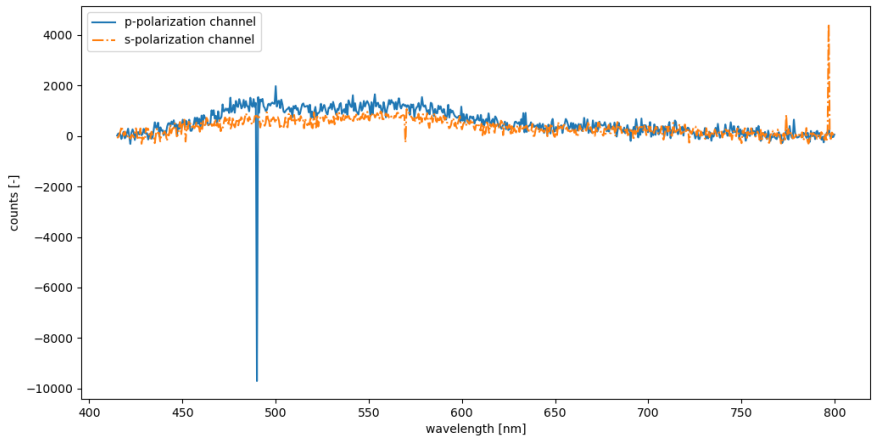


(a)

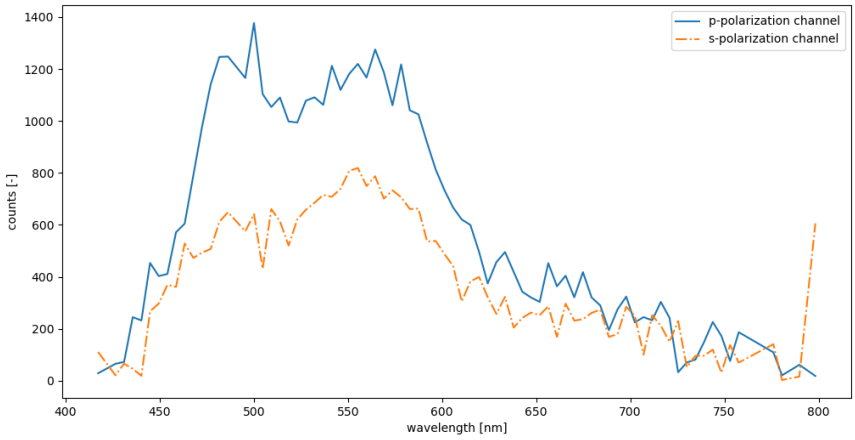


(b)

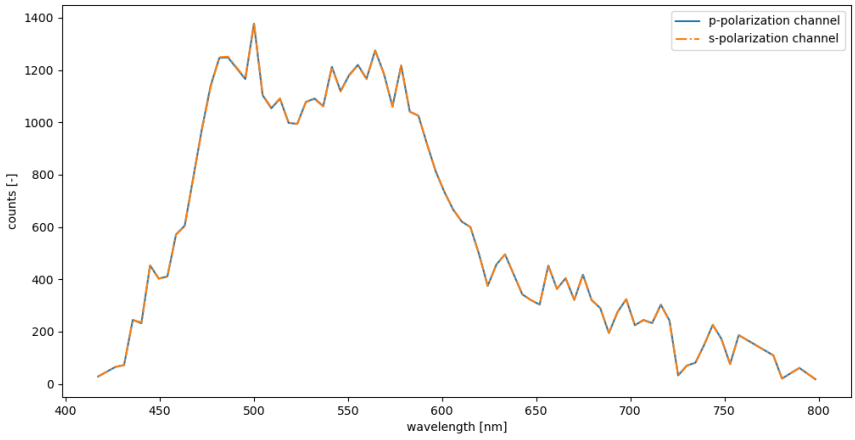


(c)

Figure 36: Observed spectrum of HD 10307 on the night of 15.07.2022. (a) shows the spectrum after dark current correction. (b) depicts the spectrum after pixel binning. (c) the final spectrum after applying the iterative transmission correction.

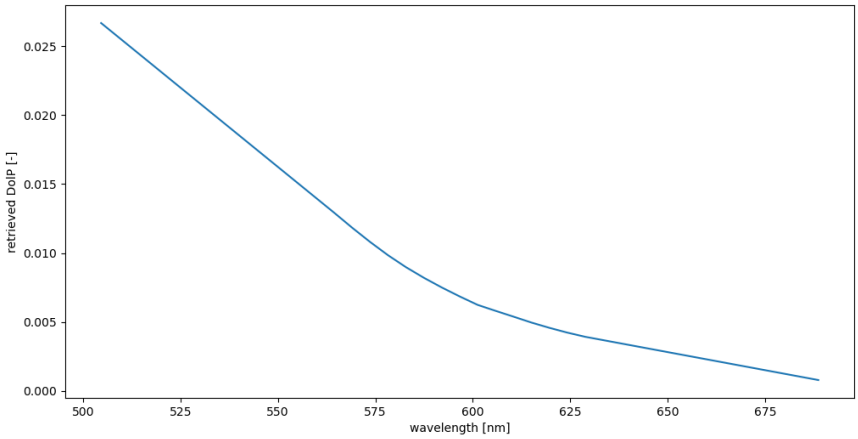


(a)

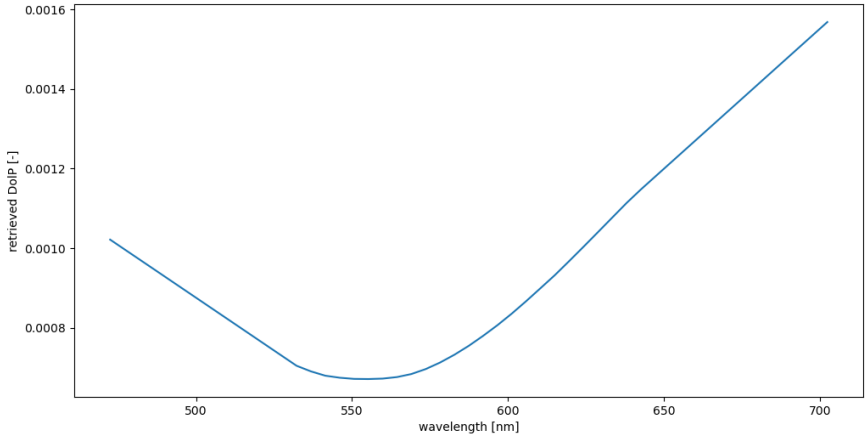


(b)

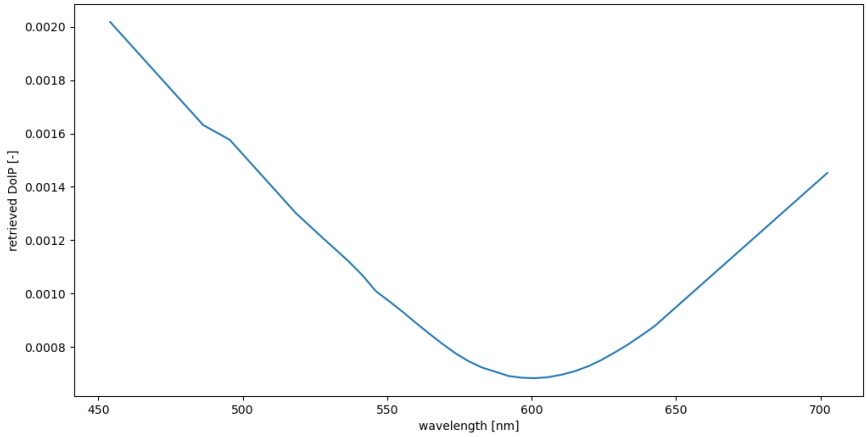


(c)

Figure 37: Retrieved DolP of observed bright stars on the night of 14-15.07.2022. (a) retrieved DolP for HD12489. (b) retrieved DolP for HD 8890. (c) retrieved DolP for HD 10307.

# 7 Conclusion

The aim of this thesis was to answer the question if spectral linear polarization modulation in the form of channelled spectropolarimetry is able to recognize Earth-orbiting resident space objects. In the first step, we stated and analysed the target GEO satellites. It was shown that the perceived movement of the satellites will not pose a problem for tracking. We clearly showed the advantage of observing GEO satellites by having a stable observation geometry. It was concluded that the phase angle has a strong impact on the visibility of the target satellites. Especially the improved apparent visual magnitude close to the minimum phase angle or glint will aid in observing the rather faint targets. We expect atmospheric extinction to reduce the received flux by up to a factor of 2.5 due to the low elevation of the target satellites from the telescope position at The Hague. We conducted a thorough photon budget estimation taking into account the throughput of the instrument and atmospheric extinction. Based on a desired SNR of 10 we estimated the needed integration time for a GEO satellite of apparent visual magnitude of 10 to be $10^1$ s for the centre wavelength at 550 nm and$10^2$ s for the red end of the spectrum. It is concluded that by using SNR improving measures like exposure stacking and pixel binning, as well as timing the observations for a minimum phase angle, we are able to take observations of GEO satellites.
We gave a detailed derivation of the modulation equation and the retrieval algorithm. We clearly showed the influence of the retardance of the multiple-order retarder on the local modulation period. This knowledge can be used for further iterations of the SSI. Additionally, we introduced a new iterative transmission correction algorithm which is able to estimate the correction channel transmission difference for the low number of modulations. For the retrieval algorithm as well as the iterative transmission correction algorithm we performed a software verification. The maximum RMS error for the iterative transmission correction algorithm was found to be 1%. This will enable future observation campaigns with the SSI to directly concentrate on the observations.
The detailed instrument description will simplify future instrument iterations. Occurred problems can be attributed to specific instrument components. It was shown that especially the used spectrograph is not suited for telescope observations and features a low efficiency as well as a prominent dark and baseline noise.
We gave a description of the possible errors and identified the effect of the slit function and the induced polarization by the telescope and the non-polarizing beamsplitter to be the most severe errors. Especially the observation geometry dependent induced polarization by the M3 mirror of the telescope requires constant calibration using known standard stars.
Wavelength and polarimetric calibration were conducted. The polarimetric efficiency calibration showed clear signs of misalignment of the quarter-wave plate and multiple order retarder. This was confirmed by a retrieved offset in the AolP. We performed validation by inducing low level DoLP using a double BK7 glass plate setup. We determined the overall laboratory polarimetric accuracy to be $\leq$ 1.2 % DolP. It was also shown that the SSI is able to distinguish DolP signals $\geq$ 1.3 % in a laboratory environment.
Due to time constraints and problems with the alignment procedure we were only able to conduct preliminary observations of bright stars. We believe that there has been a problem with the alignment, as the received photon count was around 5% of the expected one for all three observations. This is also confirmed by the varying transmission difference between both channels and additional failed observation attempts. The retrieved spectra of HD 8890 and HD 10307 were too noisy and no expected induced instrument polarization could be retrieved. The retrieved DolP of HD 124897 is within the range of the expected induced polarization and above the determined laboratory accuracy for the blue side of the spectrum. This shows the power of exposure stacking and the applied iterative transmission correction. However, it could still be an artefact of the algorithm.
Overall we were not able to answer the posed research question. Nevertheless, we took important steps toward a functioning instrument, determined possible problems, and are able to identify needed instrument iterations. We expect that this will enable the next observation campaign to be successful.

# 8 Recommendation

Based on this work there are several recommendations that should be tackled for a successful future satellite identification using the SSI.
We observed that the general bottleneck of GEO satellite observations using the SSI is the received photon flux. One of the main factors of reduced throughput is the used spectrograph including the detector. A new spectrograph with high throughput and quantum efficiency for the visual wavelength range should be considered. An important factor would also be the dark current performance to allow for higher integration times without saturation. An additional instrument change would be a new multiple-order retarder featuring increased retardance in order to increase the number of modulations and by that the resolution of the linear polarization information. This has to be tuned with the spectral resolution of the used spectrograph to avoid a strong influence of the slit function.
Another recommendation is to gain more observation-based knowledge of the atmospheric effects and the influence of the phase angle on the received photon flux. The work at hand assumed no influence of the atmosphere on the linear polarization information and took general extinction values from literature. More precise knowledge about the atmospheric extinction should be gathered by taking photometric observations with varying elevation angles and by that air mass. Additionally, photometric observations of the target satellites with varying phase angle should be conducted to induce the individual phase angles effect on the received photon flux. More spectropolarimetric measurements of standard stars should then be conducted to assess the true effect of atmospheric scattering on the linear polarization information.
The calibration and validation procedure should be repeated using the more advanced laboratory equipment used for the SPEX calibration. Additionally, radiometric calibration should be conducted in order to retrieve spectral information and by that possible material composition for future observations.
It was concluded that the discrepancy in received photon flux is probably due to a misalignment of the instrument at the telescope. To facilitate a more precise alignment, the pre-instrument optics consisting of the non-polarizing beamsplitter and tracking camera should be independently adjustable from the SSI instrument components. A bright target can then be used to mark the exact telescope focus point and adjust both parts independently for maximum throughput.
Future observations will aim to observe and identify LEO satellites using the SSI. As explained in chapter 5 this will require a continuous calibration for the telescope-induced polarization depending on the azimuth-elevation configuration. The best option is to correct for the induced polarization and phase change before the signal enters the SSI. Stokes vector cross-talk including the [V] component will induce errors in the modulation that are problematic to correct for after the signal modulation. Therefore, the Mueller matrix of the M3 mirror given by equation 35 should be determined for the whole elevation-azimuth range. A tip-tilt glass plate arrangement after the Nasmyth port opening can then be used to correct for the induced polarization. There are currently efforts at Leiden Observatory to control the spectrograph using microcontrollers. The same microcontrollers and a stepping motor could be used to control the glass plate induced correction based on the determined Muller matrix of the M3 mirror and the fed elevation-azimuth values from the tracking software of the telescope.
All named changes could lead to successful phase angle resolved spectropolarimetric measurements of satellites and their identification.

# References


[1] *Air-Spaced Doublet Collimators: FC/APC, FC/PC, & SMA*. URL: https://www.thorlabs.de/newgrouppage9.cfm?objectgroup_id=1337 (visited on 09/21/2022).

[2] *AZ800 f6.85*. Astrosysteme. URL: https://www.astrosysteme.com/products/asa-az800/ (visited on 01/09/2022).

[3] Jeremy Bailey, P. W. Lucas, and J. H. Hough. "The linear polarization of nearby bright stars measured at the parts per million level". In: *Monthly Notices of the Royal Astronomical Society* 405.4 (July 11, 2010), pp. 2570–2578.

[4] Adam Battle et al. "A Visible Spectral Atlas of Geostationary Satellites". In: Advanced Maui Optical and Space Surveillance Technologies Conference (AMOS). 2021.

[5] D. K. Beamer, U. Abeywickrema, and P. Banerjee. "Polarization vector signatures for target identification". In: Polarization Science and Remote Sensing VIII. Vol. 10407. SPIE, Aug. 30, 2017, pp. 208–214.

[6] Diane Krupp Beamer. "Polarization Signatures in Vector Space". PhD thesis. University of Dayton, 2018.

[7] Max Born and Emil Wolf. *Principles of Optics: Electromagnetic Theory of Propagation, Interference and Diffraction of Light*. Saint Louis, UNITED KINGDOM: Elsevier Science & Technology, 1980.

[8] Shane Bruski et al. "Determination of Satellite Characteristics through Visible Light Intensity Analysis". In: Advanced Maui Optical and Space Surveillance Technologies Conference (AMOS). United States Air Force Academy,Department of Astronautics,United States Air Force Academy,CO,80841, 2012, p. 9.

[9] DeAnna Maria Burt. "AMOS 2021 Conference Opening Presentation". Advanced Maui Optical and Space Surveillance Technologies Conference (AMOS) 2021, Sept. 15, 2021.

[10] Donald Bédard and Gregg A. Wade. "Time-resolved visible/near-infrared spectrometric observations of the Galaxy 11 geostationary satellite". In: *Advances in Space Research* 59.1 (Jan. 2017), pp. 212–229.

[11] Major Donald Bédard, Gregg A Wade, and Dmitry Monin. "Spectrometric characterization of geostationary satellites". In: Advanced Maui Optical and Space Surveillance Technologies Conference (AMOS). 2012, p. 11.

[12] Eric Col Felt and Joseph Col Roth. "The Space S&T Challenges fom LEO to Cislunar". AMOS 2021, Sept. 15, 2021.

[13] *Commander's Strategic Vision*. United States Space Command. URL: https://www.spacecom.mil/Mission/Commanders-Strategic-Vision/ (visited on 12/17/2021).

[14] Augustine J DeMeulenaere, Eli Q Harmon, and Francis K Chun. "Simultaneous Glint Spectral Signatures of Geosynchronous Satellites from Multiple Telescopes". In: Advanced Maui Optical and Space Surveillance Technologies Conference (AMOS). 2018, p. 10.

[15] Jack D Drummond and Richard H Rast. "First Resolved Images of a Spacecraft in Geostationary Orbit with the Keck-II 10 m Telescope". In: Advanced Maui Optical and Space Surveillance Technologies Conference (AMOS). 2010, p. 6.

[16] *Dual Wavelength Multi-Order Wave Plates*. URL: https://www.thorlabs.com/newgrouppage9.cfm?objectgroup_id=755&pn=WPDM05M-1064H-532Q (visited on 01/09/2022).

[17] Anita N. Dunsmore et al. "Spectral Measurements of Geosynchronous Satellites During Glint Season". In: *Journal of Spacecraft and Rockets* 54.2 (), pp. 349–355. (Visited on 12/03/2021).

[18] *ESO - Atmospheric Extinction*. URL: https://www.eso.org/sci/facilities/lasilla/astclim/atm_ext.html (visited on 09/21/2022).

[19] Daniel O. Fulcoly, Katharine I. Kalamaroff, and Francis K. Chun. "Determining Basic Satellite Shape from Photometric Light Curves". In: *Journal of Spacecraft and Rockets* 49.1 (Jan. 2012), pp. 76–82.

[20] Roberto Furfaro, Richard Linares, and Vishnu Reddy. "Space Objects Classification via Light-Curve Measurements: Deep Convolutional Neural Networks and Model-based Transfer Learning". In: Advanced Maui Optical and Space Surveillance Technologies Conference (AMOS). 2018, p. 17.

[21] Gorachand Ghosh. "Dispersion-equation coefficients for the refractive index and birefringence of calcite and quartz crystals". In: *Optics Communications* 163.1 (1999), pp. 95–102.
[22] Enrico Giro et al. "Polarization properties at the Nasmyth focus of the alt-azimuth TNG telescope". In: SPIE. Vol. 4843. Feb. 1, 2003, pp. 456–464.
[23] Yi Han et al. "Analysis of the optical scattering characteristics of different types of space targets". In: *Measurement Science and Technology* 25.7 (July 1, 2014), p. 075203.
[24] Michael Hart et al. "Resolved observations of geostationary satellites from the 6.5 m MMT". In: Advanced Maui Optical and Space Surveillance Technologies Conference (AMOS). 2015, p. 6.
[25] G. van Harten et al. "Atmospheric aerosol characterization with a ground-based SPEX spectropolarimetric instrument". In: *Atmospheric Measurement Techniques* 7.12 (Dec. 10, 2014), pp. 4341–4351.
[26] Gerard van Harten et al. "Prototyping for the Spectropolarimeter for Planetary EXploration (SPEX): calibration and sky measurements". In: *Polarization Science and Remote Sensing V*. Polarization Science and Remote Sensing V. Vol. 8160. International Society for Optics and Photonics, Sept. 9, 2011, 81600Z.
[27] *ILX554 pdf, ILX554 Description, ILX554 Datasheet, ILX554 view ::: ALLDATASHEET :::* URL: https://pdf1.alldatasheet.com/datasheet-pdf/view/47515/SONY/ILX554.html (visited on 09/23/2022).
[28] jessica. *Unpolarized Standard Stars*. UKIRT. URL: https://about.ifa.hawaii.edu/ukirt/calibration-and-standards/unpolarized-standard-stars/ (visited on 09/21/2022).
[29] Hans Kuiper. *Lecture Notes AE4880 Space Instrumentation Engineering*.
[30] Jack J. Lissauer and Imke de Pater. *Fundamental Planetary Science: Physics, Chemistry and Habitability*. Higher Education from Cambridge University Press. July 4, 2019.
[31] *Mounted Achromatic Wave Plates*. URL: https://www.thorlabs.com/newgrouppage9.cfm?objectgroup_id=854&pn=AQWP05M-600 (visited on 01/09/2022).
[32] Jeremy Murray-Krezan et al. "Algorithms for Automated Characterization of Three-Axis Stabilized GEOs using Non- Resolved Optical Observations". In: Advanced Maui Optical and Space Surveillance Technologies Conference (AMOS). 2012, p. 8.
[33] NATO. *NATO's approach to space*. NATO. URL: https://www.nato.int/cps/en/natohq/topics_175419.htm (visited on 12/17/2021).
[34] *Non-Polarizing Cube Beamsplitters (400 - 700 nm)*. URL: https://www.thorlabs.de/newgrouppage9.cfm?objectgroup_id=754 (visited on 09/22/2022).
[35] *Optical Spectrometers introduction*. Avantes. URL: https://www.avantes.com/support/theoretical-background/introduction-to-spectrometers/ (visited on 01/15/2022).
[36] Terry D. Oswalt and Howard E. Bond, eds. *Planets, Stars and Stellar Systems*. Dordrecht: Springer Netherlands, 2013.
[37] Vishnu Reddy. "Spectral Characterization of 2020 SO". In: Advanced Maui Optical and Space Surveillance Technologies Conference (AMOS). 2021.
[38] *Refractive index of BK7 - SCHOTT*. URL: https://refractiveindex.info/?shelf=glass&book=BK7&page=SCHOTT (visited on 09/22/2022).
[39] Murry L. Salby. *Fundamentals of atmospheric physics*. International geophysics series ; v. 61. Section: xix, 627 pages : illustrations (some color) ; 24 cm. San Diego: Academic Press, 1996.
[40] John Robert Schott. *Fundamentals of polarimetric remote sensing*. Vol. 81. SPIE press, 2009.
[41] Martijn Smit et al. "Polarimetric calibration of a spectro-polarimeter for remote sensing and characterization of aerosols". In: *International Conference on Space Optics — ICSO 2020*. International Conference on Space Optics — ICSO 2021. Ed. by Zoran Sodnik, Bruno Cugny, and Nikos Karafolas. Online Only, France: SPIE, June 11, 2021, p. 108.
[42] Frans Snik, Theodora Karalidi, and Christoph U. Keller. "Spectral modulation for full linear polarimetry". In: *Applied Optics* 48.7 (Mar. 1, 2009). Number: 7, pp. 1337–1346.
[43] *Space-Track.Org*. URL: https://www.space-track.org/auth/login (visited on 09/23/2022).
[44] Andy Speicher. "Identification of Geostationary Satellites Using Polarization Data from Unresolved Images". In: *Electronic Theses and Dissertations* (Jan. 1, 2015), p. 146.
[45] George Gabriel Stokes. *On the composition and resolution of streams of polarized light from different sources*. OCLC: 55694563. Cambridge: Cambridge Philosophical Society, 1852.

[46] Jaap Tinbergen. *Astronomical Polarimetry*. Cambridge University Press, 2005. ISBN: 978-0-521-01858-6.
[47] J.C. Toro Iniesta. *Introdcution to Spectropolarimetry*. Cambridge University Press, 2007. ISBN: 978-0-521-03648-1.
[48] T. Toyoda and M. Yabe. "The temperature dependence of the refractive indices of fused silica and crystal quartz". In: *Journal of Physics D: Applied Physics* 16.5 (May 1983). Publisher: IOP Publishing, pp. L97–L100.
[49] *Unmounted Achromatic Doublets, AR Coated: 400 - 700 nm*. URL: https://www.thorlabs.de/newgrouppage9.cfm?objectgroup_id=120&pn=AC254-100-A (visited on 01/09/2022).
[50] Daniel E Weisz et al. "Comparison of Geosynchronous Satellites Spectral Signatures During Glint Season". In: Advanced Maui Optical and Space Surveillance Technologies Conference (AMOS). 2016, p. 12.
[51] James Richard Wertz. *Mission Geometry: Orbit and Constellation Design and Management : Spacecraft Orbit and Attitude Systems*. Microcosm Press, 2001. 934 pp.
[52] James Richard Wertz, David F. Everett, and Jeffery John Puschell. *Space Mission Engineering: The New SMAD*. Microcosm Press, 2011. 1033 pp.
[53] Thomas Wijnen. *Photon Budget Estimation*. Nov. 1, 2021.
[54] *Wire Grid Beamsplitter Cube in 30 mm Cage Cube*. URL: https://www.thorlabs.com/newgrouppage9.cfm?objectgroup_id=11234&pn=CCM1-WPBS254/M (visited on 01/09/2022).
[55] *Wire Grid Polarizers on Glass Substrates*. URL: https://www.thorlabs.de/newgrouppage9.cfm?objectgroup_id=5510&pn=WP25M-VIS (visited on 01/09/2022).
[56] Andrew T. Young and William M. Irvine. "Multicolor photoelectric photometry of the brighter planets. I. Program and Procedure". In: *The Astronomical Journal* (Oct. 1967), p. 945.
[57] L A Zimmerman et al. "Near-simultaneous polarization and spectral optical measurements of geosynchronous satellites". In: Advanced Maui Optical and Space Surveillance Technologies Conference (AMOS). 2020, p. 16.